Charge Distribution Inversion for Supermicrometer Particles via Differential Mobility Analysis and Optical Particle Spectrometry

A THESIS SUBMITTED TO THE FACULTY OF THE UNIVERSITY OF MINNESOTA BY

Sarah Elizabeth Ley

IN PARTIAL FULFILLMENT OF THE REQUIREMENTS FOR THE DEGREE OF MASTER OF SCIENCE

Advised by Professor Chris Hogan

2023

Acknowledgements

This work would not have been possible without the support, knowledge, and mentoring of Professor Chris Hogan, who has been an inspiring teacher and source of encouragement for the last five years. Thank you for pushing me to grow as a researcher and student – I could not have asked for a better advisor! Thank you for the invaluable opportunity to explore undergraduate and graduate research and pursue a master's degree.

Many thanks also to Dr. José Moran, whose development of an inversion routine and assistance with data analysis, system calibration, and testing was integral to this research.

I would also like to thank my fellow lab members for making Hogan Labs productive and fun. It was a pleasure working with all of you! Thank you specifically to Dr. Souvik Ghosh, Dr. Yensil (Yeonshil) Park, and (soon-to-be Dr.) Austin Andrews, who were all incredibly patient and helpful mentors.

Finally, thank you to my parents for their constant support throughout my college career.

Abstract

Charge control of particles has long been of use for applications in laser printing, electrophotography, and electrostatic powder coating. Effective charge control is difficult, however, without an accurate understanding of particle charge state distributions. Traditional methods of charge state characterization, including the use of an average charge value, or the employment of instruments like electrodynamic balances or spectrometers, fail to robustly capture a charge distribution.

This work presents a novel approach to particle charge state characterization, using aerosol instrumentation to assess full charge state distributions for supermicrometer particles. While there are preexisting methods to discern aerosol charge state distributions, such as the Tandem Differential Mobility Analyzer approach, they are generally applied only for low charge, submicrometer particles. The method proposed here combines a Differential Mobility Analyzer (DMA) with a laser-based optical particle spectrometer capable of measuring supermicrometer-sized particle concentrations. Before selection based on electrical mobility by the DMA, particles collide with ions generated in a custom unipolar corona ionizer and become highly charged relative to what is achieved in an equilibrium charge distribution. The particles' high charge state allows them to traverse the DMA despite their large diameter. The results of this work represent the possibility to expand the applications of aerosol instrumentation into additional fields, including for use with micropowder characterization in the printing industry.

Table of Contents

Acknowledgements i

Abstract ii

Table of Figures iv

Introduction 1

Methods 11

Unipolar Ionizer 15

Data Analysis 17

Charge Distribution Inversion 19

Summary of Methods 24

Results and Discussion 25

Calibration Results - DMA 25

Calibration Results – Unipolar Ionizer 28

Experimental Results – Non-inverted Data 29

Experimental Results – Inverted Data 39

Experimental Results – Peak Charge States 51

Non-inverted ("Raw") Peak Charge States 52

Comparison of Non-Inverted and Inverted Peak Charge States 53

Discussion – Additional Considerations 57

Manipulation of Experimental Setup 57

Shape and Width of Data 59

Conclusion 61

Bibliography 64

Appendices 67

Appendix A – Dimensioned Unipolar Ionizer Schematics 67

Appendix B – Image Permissions 68

Table of Figures

Figure 1. Overview of existing charge measurement principles. (a) Millikan oil droplet method [7], (b) spectrometers [8], and (c) aerosol technology [9]. All images reproduced with permission (see Appendix B). 4

Figure 2. DMA internal operation, showing a) the trajectory of particles of different electrical mobilities and b) key parameters, including sheath flowrate, Qsh, the aerosol flowrate, Qa, the sampled aerosol, Qsa, and the exiting (non-selected) aerosol, Qex. Also shown are the DMA dimensions: length L, inner radius r1, and outer radius r2. Voltage V is applied to the center rod (inner radius), while the outer radius is grounded [Reproduced with permission, 11]. 6

Figure 3. Experimental schematic. Particles are generated in atomizer, conditioned via a series of diffusion driers, and charged via collision with ions generated in a custom unipolar corona ionizer. The flow is balanced using a pump, and particle selection and analysis occurs via the combination of a DMA operating at a fixed voltage and transporting particles of a given mobility, and an OPS measuring particle concentration as a function of particle size. 13

Figure 4. Unipolar ionizer. A high DC voltage was applied to a sharpened tungsten needle in the center of the ionizer while compressed air was passed through a series of small holes, creating an air jet. After forming a jet, the air molecules were attracted towards the tip of the needle, where the voltage was most concentrated, and separation of the air ions occurred via corona discharge. The ions were accelerated out of the ionizer using a critical orifice, where they combined with the particle flow. 16

Figure 5. Experimental schematic for calibration testing. Particle are generated in an atomizer and conditioned using a series of diffusion driers. An equilibrium distribution of charge states (consisting primarily of 0, ± 1, and ± 2) is applied with a Po-210 neutralizer source. Particles are selected and analyzed using a combination of a DMA and a CPC. 26

Figure 6. DMA calibration conducted with 200 nm PSL particles having a Boltzmann charge distribution, as applied by a Po-210 neutralizer. The (a) applied DMA voltage and (b) associated mobility diameter are shown. The singly charged, singlet peak can be observed at 2.3 kV, or a mobility diameter of 200 nm, as expected for calibration with a 200 nm PSL size standard solution. The dimer can also be observed at approximately 3.4 kV, or a mobility diameter of 260 nm. 27

Figure 7. Unipolar ionizer current as a function of supply voltage. Consistent current behavior was observed between applied voltage of 5 and 6 kV, with resulting currents of 3 to 14 μA. Below 4.95 kV, there was no discernable ionizer current, while beginning at 6.18

kV, sparking began to occur. The current was measured every 25 volts, with data points recorded each time the current increased to the next unit value.....29

Figure 8. Raw number concentration curves as a function of voltage applied to the DMA, for ionizer operating at a current of 9 μA. These plots show the "raw" data, or the non-inverted dataset, which does not include the effects of the DMA transfer function. 31

Figure 9. Raw number concentration curves as a function of voltage applied to the DMA, for ionizer operating at a current of 10 μA. These plots show the "raw" data, or the non-inverted dataset, which does not include the effects of the DMA transfer function. 32

Figure 10. Raw number concentration curves as a function of voltage applied to the DMA, for ionizer operating at a current of 12 μA. These plots show the "raw" data, or the non-inverted dataset, which does not include the effects of the DMA transfer function. 33

Figure 11. Raw number concentration curves as a function of calculated state of charge, for ionizer operating at a current of 9 μA. These plots show the "raw", or non-inverted dataset, which does not include the effects of the DMA transfer function.....36

Figure 12. Raw number concentration curves as a function of calculated state of charge, for ionizer operating at a current of 10 μA. These plots show the "raw", or non-inverted dataset, which does not include the effects of the DMA transfer function.....37

Figure 13. Raw number concentration curves as a function of calculated state of charge, for ionizer operating at a current of 12 μA. These plots show the "raw", or non-inverted dataset, which does not include the effects of the DMA transfer function.....38

Figure 14. DMA transfer function, as determined for the six tested particle sizes. The transfer functions shown were found at a fixed voltage of 4 kV, and are meant to demonstrate the increasing effect of the transfer function with increasing particle diameter; however, they are not meant to be numerically representative, as the transfer function changes with system characteristics included applied DMA voltage.....40

Figure 15. L-curve criterion for 9 μA ionizer, used to determine an optimal regularization parameter, α, for use with each particle size in the inversion process. The optimal solution value was determined by minimizing the residual of the inversion matrix problem, Ax-b. ...42

Figure 16. L-curve criterion for 10 μA ionizer, used to determine an optimal regularization parameter, α, for use with each particle size in the inversion process. The optimal solution value was determined by minimizing the residual of the inversion matrix problem, Ax-b. ...43

Figure 17. L-curve criterion for 12 μA ionizer, used to determine an optimal regularization parameter, α, for use with each particle size in the inversion process. The optimal solution value was determined by minimizing the residual of the inversion matrix problem, Ax-b. ...43

Figure 18. Inverted charge fraction curves as a function of elementary charge state, for ionizer operating at a current of 9 μA. 45

Figure 19. Inverted charge fraction curves as a function of elementary charge state, for ionizer operating at a current of 10 μA. 46

Figure 20. Inverted charge fraction curves as a function of elementary charge state, for ionizer operating at a current of 12 μA. 47

Figure 21. Charge fraction for 2 μm particles, showing both non-inverted ("raw," represented by square symbols) and inverted (represented by circular symbols) data, for an ionizer current of a) 9 μA, b) 10 μA, and c) 12 μA....48

Figure 22. Non-inverted peak charge as a function of size for ionizer operating at a current of 9 μA. 52

Figure 23. Non-inverted peak charge as a function of size for ionizer operating at a current of 10 μA. 52

Figure 24. Non-inverted peak charge as a function of size for ionizer operating at a current of 12 μA. 53

Figure 25. Non-inverted and inverted peak charge as a function of size for 9 μA ionizer. The peak charge state was determined using interpolation of the charge fraction distributions. ...53

Figure 26. Non-inverted and inverted peak charge as a function of size for 10 μA ionizer. The peak charge state was determined using interpolation of the charge fraction distributions. 54

Figure 27. Non-inverted and inverted peak charge as a function of size for 12 μA ionizer. The peak charge state was determined using interpolation of the charge fraction distributions. 54

Figure 28. Lower bound of charge state, presented as a function of particle size. Data is shown for a DMA where the max operating voltage is 7, 8, and 10 kV. The attainable charge states are shaded, illustrating that above the lines for each voltage, all charge states for a given particle size could be transmitted and analyzed. Below the lines, transmission is not possible, per DMA theory (Equations 1-4). 58

Figure 29. Lower bound of charge state, presented as a function of particle size. Data is shown for a DMA with a length of 44 cm (standard long-DMA length), 88 cm, and 100 cm. The attainable charge states are shaded, illustrating that above the lines for each voltage, all charge states for a given particle size could be transmitted and analyzed. Below the lines, transmission is not possible, per DMA theory (Equations 1-4). 59

Introduction

Charge control of micropowders has recently gained interest for applications in a variety of industries, including for use in processing techniques such as laser printing, electrophotography, and electrostatic powder coating [1]. In these applications, the toner powder generally requires a uniform charge for deposition on the printing surface. The challenge then lies in unifying the powder charge to a controlled value, which is often accomplished using a charge control agent, or "charge carrier" [2]. Tribocharging, or the transfer of surface (electrical) charge through contact and subsequent separation, is the method most frequently used to transfer charge from the charge carrier to the powder. This often occurs in powders when a charge carrier is mixed with the powder; charges then accumulate on the surface of the powder particles [1]. These charge carriers frequently have magnetic properties, in addition to their charge, which allows them to be pulled away from the powder particles using a magnetic brush drum. Powder particles are then pulled to a printing transfer roll by an electric field, where they will be deposited in the desired pattern for the printed image. For this process to be successful, the charge of the powder needs to be unipolar, such that most of the powder particles are pulled to the printing transfer roll for deposition. The abilities to charge the particles and to control their charge state are therefore the "most important properties" of these processes [2]. To ensure the powder can be efficiently deposited, thorough charge characterization of the tribocharged particles is vital.

One of the first investigations of particle charging was conducted by Robert Millikan, who used an electrodynamic balance to determine individual particle charge states, and eventually identified the unit electron charge [3]. Millikan's electrodynamic balance used two

electrodes to suspend a particle, with one electrode placed above and the other placed below the particle (Figure 1a). Conventionally, electrodynamic balances use an "adjustable DC electric field" to keep a charged particle vertically suspended between two electrodes, against the force of gravity; an AC electrical field "stabilizes the particle dynamically" [4]. This method allows information on the particle's thermodynamic and material properties to be gathered. While an electrodynamic balance is effective for the analysis of large-diameter particles (the modern electrodynamic balance can often accommodate particles from 0.3 to 300 μm), it generally requires particle-by-particle analysis, making it a slow process, and impractical to assess the charge state of concentrated particle flows. It is also difficult to adapt the method for use with polydisperse particles. Obtaining a charge distribution typically requires a determination of both the particle size distribution and the charge distribution for a flow of particles. Alternatively, the particle sizes can be controlled, and the charge states measured, to understand how a process affects the known-sized particles.

Current methods of charge characterization are often limited to the determination of a net charge state, or average charge, particularly for micrometer-sized particles [5-6]. These net charge approaches include the Faraday cage method, which involves the measurement of a net charge for particles within a metal enclosure; the charge is measured via an electrometer [5]. Average particle charge levels can also be estimated theoretically based on the materials and electric field levels used in a testing apparatus [6]. Limited instruments for the measurement of electrostatic charge distributions on toner powders have been developed, such as the E-SPART (electrical-single particle aerodynamic relaxation time) analyzer [5]. This instrument uses a laser to assess aerodynamic diameter in the range of 0.3 to 70 μm. An

acoustic excitation with an applied dc electric field is then used to determine electrostatic charge (magnitude and polarity) on a particle-by-particle basis. One limitation of the instrument is its inability to measure particle electrostatic charge beyond the dynamic range of 0 to +/- 20 uC/g, due to "appreciable particle loss" above this level of charge [5]. The ESPART is one of the only instruments with the capacity to characterize both aerodynamic diameter and charge in a time-effective manner; however, it has not been widely implemented in charge characterization efforts.

a)

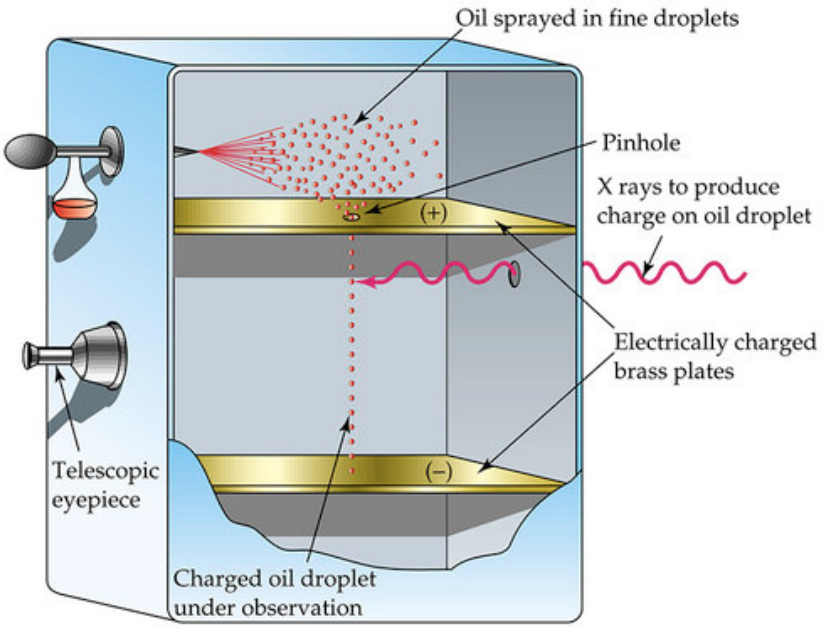

b)

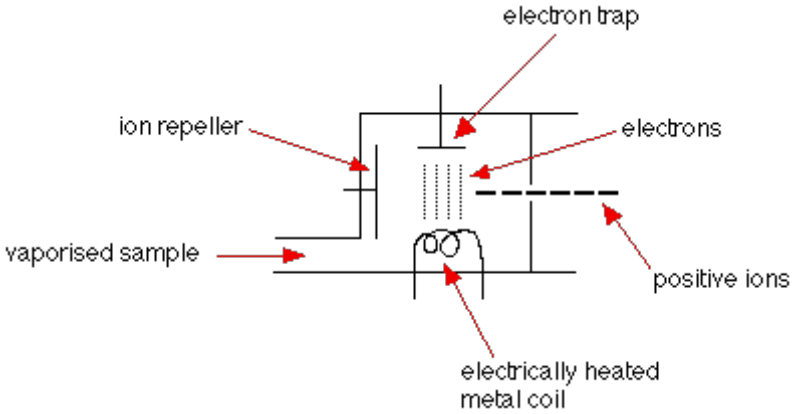

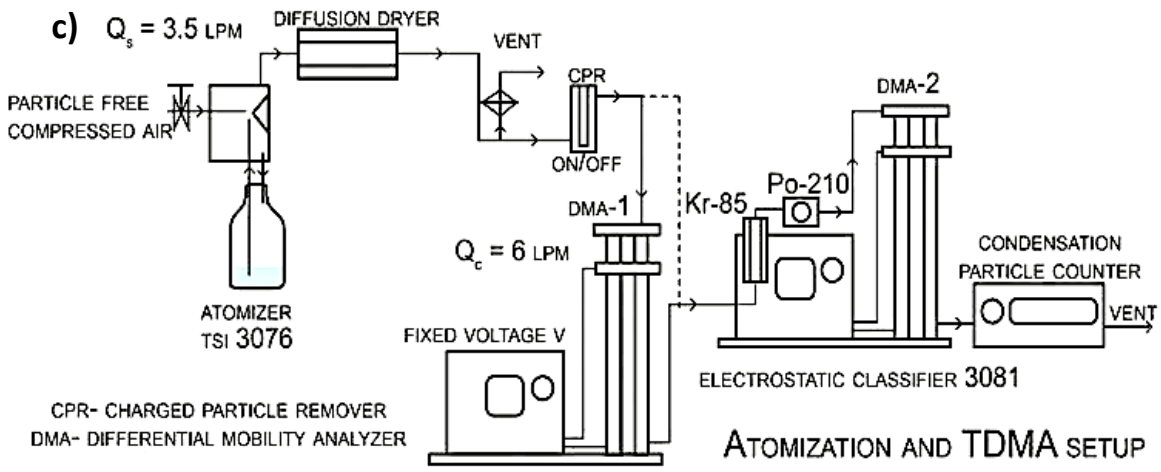

Figure 1. Overview of existing charge measurement principles. (a) Millikan oil droplet method [7], (b) spectrometers [8], and (c) aerosol technology [9]. All images reproduced with permission (see Appendix B).

Charge spectrometers are additional instruments that can be used for charge characterization, which deflect particles according to their mass and charge (Figure 1b). Epping (2002) used a free air beam spectrometer to evaluate the charge-to-mass ratio for 1 to 200 μm particles [10]. Since spectrometry methods provide only the charge-to-mass ratio, they generally fail to capture a detailed charge distribution measurement, as they are unable to decouple particle mass and particle charge state. They are also generally used only for low-charge particles. To promote uniform powder charge and distribution, it is desirable to develop an independent understanding of both properties, ideally using a single process.

Although only a few methods have been demonstrated for charge distribution measurements of particles larger than 1 μm, charge characterization has been well-documented for submicrometer aerosol particles, as shown subsequently. These existing, well-established methods, such as the use of tandem Differential Mobility Analyzers (TDMA analysis), can be extended to the charge characterization of large-diameter particles such as powders.

Differential Mobility Analyzers (DMAs) consist of two concentric metal cylinders. The central cylinder is a rod that is operated at a given positive or negative voltage, generating an electric field in the gap between the two cylinders. Particles enter at the top of the instrument, as shown by the particle trajectory in Figure 2b, and are drawn towards or repelled by the center rod, depending on the polarity of their charge. They simultaneously follow the path of a sheath flow, which passes from the top to the bottom of the instrument. The sheath flow is controlled by a blower and power supply, with a mass flow meter continuously monitoring the flowrate. The sheath flow is composed of clean, filtered air. As a combination of electrodynamic and drag forces act on the particles, they follow distinct trajectories (Figure 2a) depending on their electrical mobility, which is the proportionality constant between the particle terminal velocity and the external electric field and is a function of the particle physical size and charge state. For particles of an equivalent charge, the smaller particles will tend to adhere to the central rod, while larger particles will tend to impact at the bottom of the instrument, which is shown in Figure 2a. Only the particle with the selected electrical mobility will reach the central rod at the same point when it reaches the base of the instrument, allowing it to exit the instrument and continue through the flow system for further analysis [11]. The DMA operational principle is shown in Figure 2.

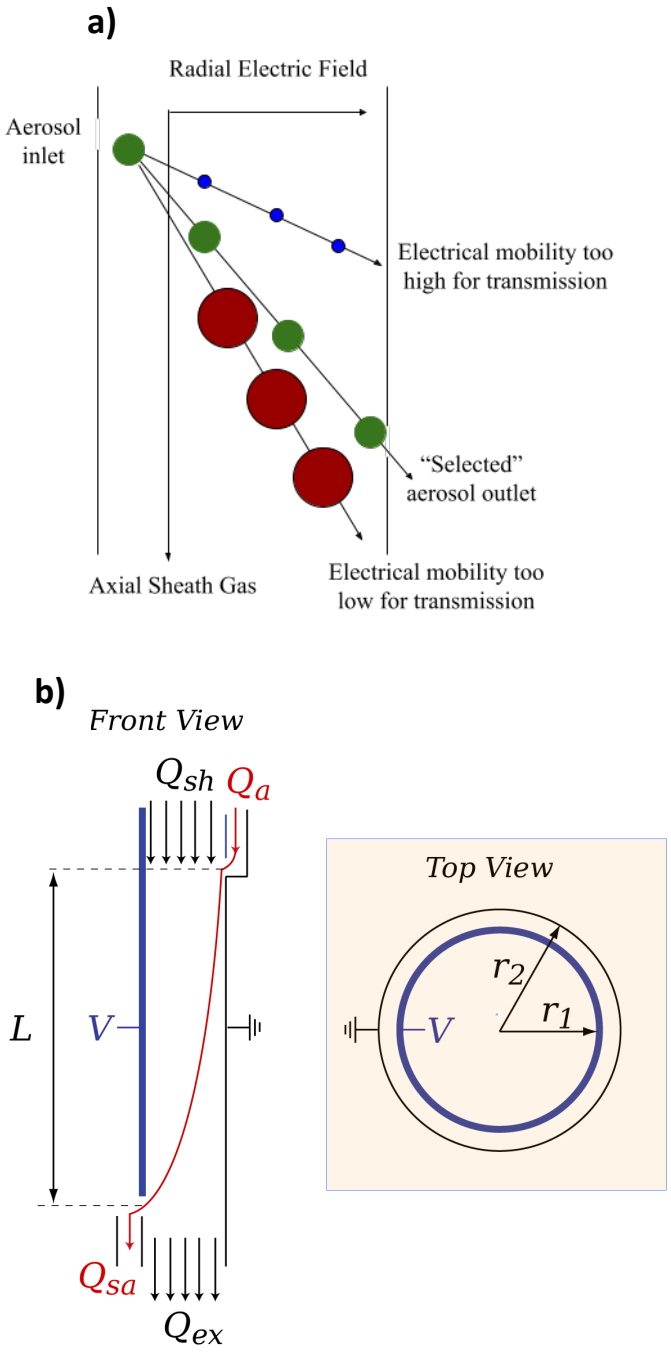

Figure 2. DMA internal operation, showing a) the trajectory of particles of different electrical mobilities and b) key parameters, including sheath flowrate, Qsh, the aerosol flowrate, Qa, the sampled aerosol, Qsa, and the exiting (non-selected) aerosol, Qex. Also shown are the DMA dimensions: length L, inner radius r1, and outer radius r2. Voltage V

is applied to the center rod (inner radius), while the outer radius is grounded [Reproduced with permission, 11].

The TDMA method of particle analysis involves the use of two DMAs, with one operating at a fixed voltage, selecting a certain electrical mobility. For most applications, the desired particles will be of a single charge, so the first DMA is selecting aerosols of a known size since the charge state is fixed. The second DMA will generally "scan" through a series of voltages, collecting a distribution of a given characteristic. For instance, Liu et al. (1978) used TDMA analysis to measure the growth of particles due to air humidity: the first DMA generated a monodisperse aerosol, while the second DMA gathered a size distribution following the particle growth [12]. A tandem DMA system has also been used to eliminate multiply charged particles; the second DMA is used to reclassify the aerosol flow, removing multiply charged particles that were able to pass through the first DMA [13]. The aerosol field has a significant history of similar characterization using the TDMA approach, including Knutson (1976), Hoppel (1978), Fissan et al. (1982), Plomp et al. (1982), Scheibel et al. (1983), and Kousaka et al. (1985) [14-19]. The TDMA method has been used selectively for charge analysis of particles, as was done by Sahu, Park, & Biswas (2012), among others [20]. For their analysis, the first DMA was operated at a fixed voltage and used to classify particles of equivalent mobility, and the selected particles were then neutralized. The second DMA scanned through voltages, selecting a given particle size at each voltage, and a Condensation Particle Counter was used to measure a particle size distribution. The results showed that particles were either singly or doubly charged, with the charge fraction dependent on particle size and the addition of a copper dopant. This method of measuring charge distribution has historically been effective for particles of low charge but is then limited in the particle sizes which it can capture.

Existing methods of analysis which employ DMA systems have primarily been used for submicrometer particles, generally in the range of 10 to 300 nm, as was the case for Biskos et al. (2005) [21].

The charge distribution of monodispersed particles has also been assessed using TDMA analysis for particles charged with unipolar diffusion [21]. Unipolar charging methods were of interest to this investigation, as they were the intended method of attaining a high electrical mobility on tested particles. Similar unipolar charge distributions have been obtained by Kaminski et al. (2012) and Järvinen et al. (2017), while Domat et al. (2014) developed a theoretical model for unipolar charging [22-24]. TDMA systems have been selectively used for particles that were charged bipolarly, as in Liu and Pui (1974) and Maricq (2008) [25, 26]. Another approach to charge state analysis that has been used combines several instruments: the Aerodynamic Aerosol Classifier offers an "all-in-one" method of characterization [27].

Depending on the testing application, particle concentrations can be measured by laser particle counters such as Condensation Particle Counters (CPCs) or Optical Particle Sizers (OPSs), or using an Aerodynamic Particle Spectrometer (APS), after DMA particle selection. Biermann and Bergman (1984) combined a DMA and Optical Particle Counter, or OPC [28]. Additionally, a DMA-to-spectrometer system can be used, as was done by Emets, Kascheev, & Poluektov (1991), and Forsyth, Liu, & Romay (1998) [29-30]. All three of these investigations were able to obtain simultaneous charge and size distribution measurements; however, data for supermicrometer particles is limited, with most results falling in the submicrometer range. For instance, in Biermann & Bergmann, data is primarily for 0.5 and 0.8 μm monodisperse solutions, with only one result shown for supermicrometer particles [28].

Similarly, in Emets, Kascheev, & Poluektov, the maximum diameter measured was 2 μm, with relatively low particle charges and limited data available [29]. The experiments of Forsyth, Liu, & Romay were also limited to submicrometer particles, with select instances of data for particles up to 2 μm in diameter [30]. In all cases, the effects of the DMA transfer function were neglected.

Traditional charge characterization methods for aerosols have historically been overlooked for use with particle charge characterization, as most micropowders and other novel materials are of supermicrometer size. While there are a few notable exceptions, available data for aerosol instrumentation at larger particle sizes tends to be limited, with experimental data available primarily for submicrometer particles and select instances of data for particles up to 2 μm in diameter. Additionally, existing charge distributions may not be accurate, as they do not account for the DMA transfer function through an inversion process. The transfer function governs which particles will successfully traverse an electrostatic classifier such as the DMA; the use of a proper data inversion scheme was a key focus of this work that necessarily manipulates the charge distribution data to ensure its accuracy.

The objective of this investigation is to build upon existing aerosol-based charge distribution measurement techniques, developing a method of charge state determination for supermicrometer-sized particles. Monodisperse solutions of Polystyrene Latex (PSL) were generated and unipolarly charged with a custom ionizer set to one of three tested operating currents. Particle sizes from approximately half a micrometer to three micrometers were tested with three different ionizer currents. The charge state was generally expected to increase as a function of the ionizer current, due to more ions being produced. A

determination of particle charge state was then accomplished via the coupling of a DMA and an Optical Particle Spectrometer (Size), or OPS. The DMA selected a single electrical mobility, and the OPS was capable of "binning" particles by size, allowing the particle charge state distribution to be extracted from system operating information for a given particle size. Following data collection, an inversion routine was used to account for the transfer function of the DMA. The use of a data inversion was an important advancement beyond previous work, as the transfer function can have a significant effect on the charge state. The effect of the transfer function is especially significant for the larger tested particle sizes, for which only limited charge distribution data is currently available. The proposal of a combined DMA and OPS system, used with a robust data inversion scheme, makes this investigation a novel departure from previous work and aims to demonstrate the possibility of applying aerosol instrumentation to unexplored areas, including the charge characterization of supermicrometer particles.

Methods

A system for the determination of a charge state distribution as a function of particle size was devised using the combination of a Differential Mobility Analyzer (DMA) and an Optical Particle Spectrometer (OPS). While typically used for singly charged, submicrometer particles, the DMA is capable of transporting supermicrometer particles provided their electrical mobility falls within the system operating limits, as governed by DMA theory. The OPS is capable of measuring particle concentrations for particles between 0.3 and 10 μm in diameter. The use of these two seemingly incongruous instruments was meant to demonstrate their application to highly charged, supermicrometer particles. As explained subsequently, monodisperse particle solutions were generated such that they would be detected in a single particle size range "bin" of the OPS; the particles were then charged through collisions with ions in a unipolar ionizer. A series of voltages were applied to the DMA, with each corresponding to a given electrical mobility. After transmitting through the DMA, particle concentrations were measured by the OPS. Using the known particle diameters, the particle charge states were calculated using DMA theory, and the data were appropriately adjusted with an inversion scheme. Figure 3 shows the combined DMA-OPS experimental schematic.

For experimental charge distribution measurements with the DMA-OPS system, Polystyrene Latex (PSL) particles were generated in a custom collision-type atomizer modeled after the operating principle of the TSI Atomizer Model 3076, with clean compressed air provided to the atomizer at 40 psi for aerosolization. Fisher Scientific (Duke Standards) NIST-certified PSL suspensions in diameters of 490 nm, 800 nm, 1 μm, 1.6 μm, 2 μm, and 3 μm were tested. These solutions are extremely monodisperse, with nominal diameters of 0.49 μm (with

unknown variance), 803 ± 14 nm, 1.025 ± 0.01 μm, 1.592 ± 0.016 μm, 2.020 ± 0.015 μm, and 2.994 ± 0.031 μm, respectively, as specified by the manufacturer. For the 0.49, 0.8, and 1.0 μm solutions, 10 drops of concentrated PSL solution were dissolved in 40 mL of pure, deionized water. To achieve higher particle concentrations, 30 drops of PSL per 40 mL H_2O were used to generate the 1.6, 2, and 3 μm particles. The primary concern of the investigation was relative concentration, for the purpose of identifying the DMA voltage at which a peak concentration was observed. It was therefore desirable to ensure particle concentrations reached levels such that there was a clear distinction between voltages with "low" and "high" concentrations. The actual particle concentration was not vital, as concentrations for particles larger than 1 μm drop dramatically due to losses.

After aerosolization, the generated droplets, containing monodisperse particles, passed through two diffusion driers filled with Dry & Dry brand Blue Indicating Silica Gel Beads; the driers removed excess water from the particles. The beads were replaced once they began to lose their blue color, which would indicate an excess water concentration within the beads. A custom-designed unipolar ionizer (see "Unipolar Ionizer") was used to generate positively charged ions, which were accelerated through a size 28 O'Keefe Controls critical orifice and mixed with the aerosol particle flow. The current of the produced ions was continuously monitored using a ZHFU 85C1 ammeter connected to earth ground. The ion and particle flows were mixed using a tee connector. The ions generated in the ionizer combined with the aerosol flow, and the ions were able to unipolarly charge the dried PSL particles through random collisions caused by Brownian motion [31]. Following these collisions, the PSL particles obtained additional unit charges, beyond what is achievable with an equilibrium charge

distribution. This process significantly increased the number of unit charges on the PSL particles, which subsequently increased their electrical mobility. Ionizer currents of 9, 10, and 12 µA were tested for each PSL particle size, with an increase in the production of ions being associated with a higher corona current. It was theorized that this would increase the probability of particles achieving higher charge states, as they would have the opportunity to receive charge from a higher number of ions and ion collisions.

Following the ionizer, a constant-flow MSP Corporation pump pulled away approximately 0.73 liters per minute, balancing the flow before the particles continued to a Differential Mobility Analyzer (DMA). A size 17 critical orifice was used to choke the flow, and an adjustable valve allowed for control of the pump exhaust flow. The removal of a set amount of flow was meant to eliminate the possibility of overloading the DMA or subsequent instruments with particles.

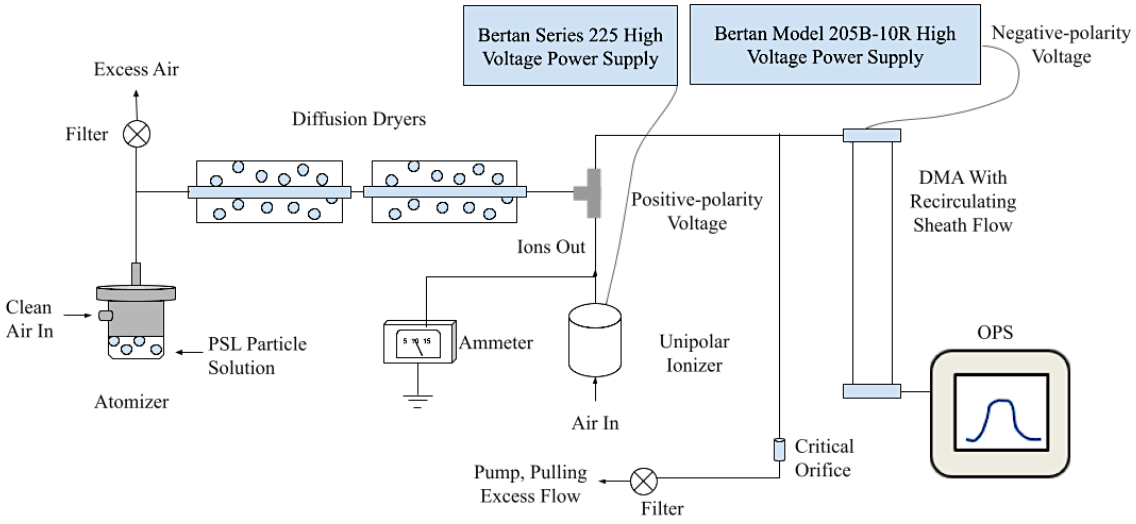

Figure 3. Experimental schematic. Particles are generated in atomizer, conditioned via a series of diffusion driers, and charged via collision with ions generated in a custom unipolar

corona ionizer. The flow is balanced using a pump, and particle selection and analysis occurs via the combination of a DMA operating at a fixed voltage and transporting particles of a given mobility, and an OPS measuring particle concentration as a function of particle size.

The DMA maintained a flowrate ratio of approximately 4:1, with a sheath flowrate of 4.10 lpm provided by recirculating airflow within a custom blower system. The sheath flowrate was monitored throughout testing using a TSI 4000 Series flowmeter and could be adjusted with a current-controlled Kungber power supply. Two Eta HC21-4N HEPA capsule filters were used to ensure the sheath flow remained free of any particulate. A Bertan Associates, Inc. Series 205B – 10R power supply provided a negative polarity voltage to the DMA, with a voltage limit of 7.3 kV. After aerosol flow of a single electrical mobility exited the DMA, a TSI Model 3330 Optical Particle Sizer (OPS) was used to pull aerosol flow through the DMA at a rate of 1.0 liter per minute. The OPS uses laser diffraction to measure the optical diameter of collected particles, with the direction of scattered light reliant on the particle size, causing a certain intensity of scattered light to be detected and converted to size. The measured particles are "binned" by the instrument according to their measured size, and within each bin, a real-time particle concentration is displayed and averaged. Particle size was constant, due to the monodispersity of the PSL solutions; since the size was known, the size bin of interest could be isolated from the OPS data, providing relative particle concentrations for each of the tested PSL sizes. The DMA voltage was stepped from 0 to approximately 6.5 kV, with two-minute OPS continuous measurements collected at each voltage. From 0 to 2 kV, measurements were taken every 100 volts, while beyond this point, measurements were taken every 250 volts. For voltages 4 kV and above, measurements were taken every 500 volts. This measurement

scheme allowed for more efficient data collection while ensuring data resolution near the points where concentration peaks occurred for all tested particle sizes, which was always below 2 kV. Each sample outputted an average value over the two-minute sampling, and at each voltage data points were taken in duplicate and averaged.

Unipolar Ionizer

A unipolar ionizer, hereafter "ionizer", was developed based on existing ion generators, which have been demonstrated for use as particle chargers. A key inspiration was the system developed by Whitby (1961), which can be found in Intra et al. (2011), Figure 5 [32, 33]. The purpose of the ionizer was to generate ions from air molecules; the ions would then be used to apply a high charge to the particles. The ionizer was developed and manufactured with assistance from the University of Minnesota College of Science and Engineering Machine Shop. Figure 5 shows a cutaway view of the ionizer; a dimensioned ionizer schematic can be found in Appendix A.

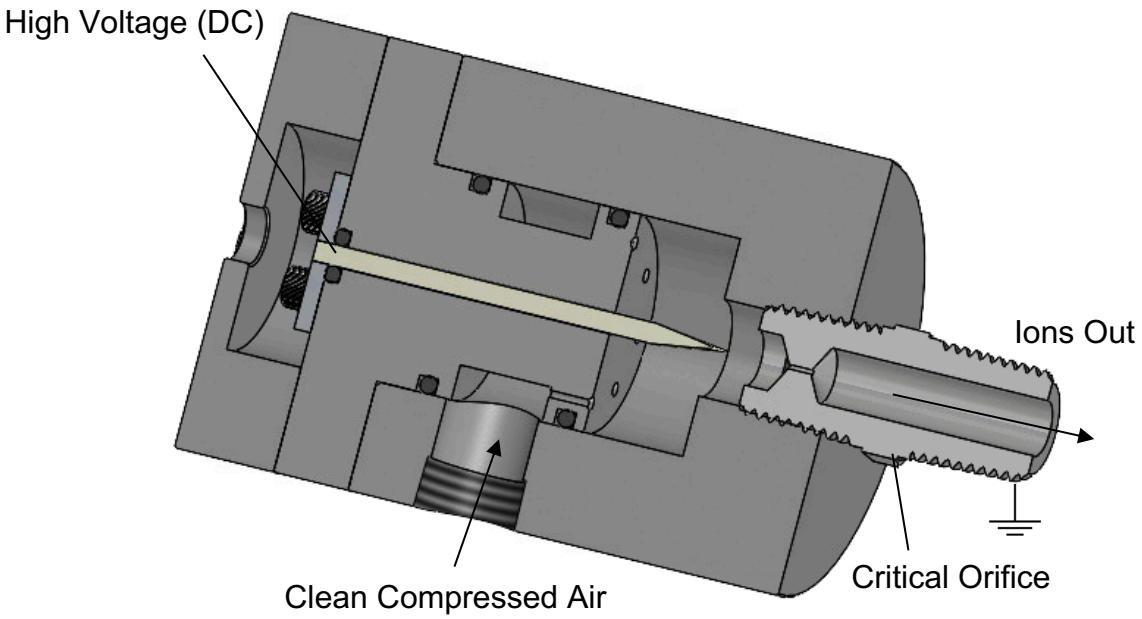

Figure 4. Unipolar ionizer. A high DC voltage was applied to a sharpened tungsten needle in the center of the ionizer while compressed air was passed through a series of small holes, creating an air jet. After forming a jet, the air molecules were attracted towards the tip of the needle, where the voltage was most concentrated, and separation of the air ions occurred via corona discharge. The ions were accelerated out of the ionizer using a critical orifice, where they combined with the particle flow.

A pure tungsten welding needle was sharpened to a point of approximately 15 degrees and enclosed in a cylindrical housing. A Bertan Series 225-20 high voltage power supply was used to supply a positive D.C. voltage of either 5.65, 5.84, or 5.975 kV to the needle, resulting in a current of 9, 10, or 12 μA, respectively. The current range of the ionizer was 3 to 14 μA, requiring an applied voltage of approximately 5 to 6 kV. Beyond this range, the ionizer began to spark. The ionizer current was continuously measured through a ZHFU Model 85C1 ammeter connected to earth ground.

To provide gas in which ions could be generated, compressed air was passed through an Eta HC06-4N HEPA capsule filter and supplied to the ionizer. Within the instrument, the air passed through a series of eight 1/32" holes in the direction of the needle. The small hole size and uniform patterning accelerated the air into a jet and forced it toward the needle tip from multiple directions. The current at the tip of the needle reached a level sufficient to generate a corona discharge, which attracted the air and subsequently ionized the air molecules. The sharp point of the needle was meant to concentrate ions, pulling a maximum number of them away from the smooth needle body. The ions were then accelerated through a size 28 O'Keefe Controls critical orifice at approximately 0.727 liters per minute, where they mixed with the particle flow through random collisions occurring within a tee connector. The ions accepted by the particles could significantly increase their charge states.

Data Analysis

As mentioned above, monodispersed particle solutions were used for this investigation, meaning that the relevant particle data always fell into a single OPS "bin". Since the DMA outputs particles of a single electrical mobility (combination of both particle size and charge), the use of a size-characterizing instrument was important to ensure only the data for the desired particle size was extracted and analyzed. Furthermore, to attain optimal data resolution, the default size bins of the OPS surrounding the particle size of interest were manipulated to be as narrow as possible. The remaining bins were left as their default values. For the 0.49 and 0.80 μm solutions, the selected bins were 0.02 and 0.04 μm in width, respectively. For the 1, 1.6, and 2 μm solutions, the OPS bins were made to be 0.2 μm in width, while the 3 μm PSL solution had a bin width of 0.5 μm.

Once the particle data was collected, the average particle concentration at each DMA voltage was determined (samples were taken in duplicate at each voltage). Since the particle size was known, the theoretical particle mobility could be calculated based on the applied DMA voltage for each data point, using Equation 1:

$$Z_p^* = \frac{Q_{sh}+Q_{ex}}{4\pi V L_{eff}} \ln\left(\frac{r_2}{r_1}\right) \quad [1]$$

Where Z_p^* is a set electrical mobility, Q_{sh} is the entering sheath air flow rate, Q_{ex} is the main outlet flow rate, V is the voltage applied to the DMA, and L_{eff} is the effective length of the DMA, or the length between the exit slit and polydisperse aerosol inlet [34]. L_{eff} is prescribed to be 44.369 cm, as described in the TSI Series 3080 Electrostatic Classifiers Operation and Service Manual, Revision J (2009) [35]. The values r_2 and r_1 are similarly available in the TSI 3080 Service Manual, and describe the inner and outer physical radii of the DMA. The outer radius of the annular space of the DMA, r_2, is 1.961 cm, while the inner radius of the annular space, r_1, is 0.937 cm. Similarly, Equation 2 provides a method of determining the electrical mobility of the selected particle, given its size and charge state:

$$Z_p^* = \frac{zeC_c}{3\pi\mu d_p} \quad [2]$$

Where z is the number of elementary charges on the particle, e is the elementary charge ($1.6 * 10^{-19}$ Coulomb), C_c is the Cunningham slip correction factor (defined mathematically, below), μ is the gas viscosity (taken to be $18.5 * 10^{-6}$ kg/m•s for air at STP), and d_p is the physical particle diameter.

The Cunningham slip correction factor is a dimensionless number that allows the drag force on a particle moving through a fluid to be predicted. The correction factor is given by:

$$C_c = 1 + Kn\left[\alpha + \beta \exp\left(-\frac{\gamma}{Kn}\right)\right] \quad [3]$$

Where Kn is the Knudson number, and $Kn = \frac{2\lambda}{d_p}$. λ is the gas mean free path, which is 66.5 nm in air. Depending on the testing conditions, specifically the room temperature, the mean free path may vary slightly. As in the equations above, d_p is the particle diameter. The remaining values in Equation 3 are defined in Allen & Raabe (1985), where α is 1.142, β is 0.558, and γ is 0.999 [36].

By combining Equations 1 and 2, for which the electrical mobility values (Z_p^*) are equal, the theoretical charge state, z, of a particle of known size, selected at a given DMA voltage, could be determined, using Equation 4:

$$z = \frac{3\mu(Q_{sh}+Q_{ex})d_p}{4C_c eVL_{eff}} \ln\left(\frac{r_2}{r_1}\right) \quad [4]$$

This was done for each DMA voltage, providing a data set of charge state versus measured particle concentration. For each tested particle size, the point for which a peak concentration was observed was considered the dominant charge state for that particle size.

Charge Distribution Inversion

A more robust inversion process was used to verify the dominant charge state for each particle size and determine the charge fraction as a function of the number of elementary charges.

While previous investigations, namely Biermann and Bergman (1984), Emets, Kascheev, and Poluektov (1991), and Forsyth, Liu, and Romay (1998), obtained charge distributions using a similar coupled experimental system, their results did not account for the DMA transfer function [28-30]. An inversion process properly accounts for all DMA properties, particularly the transfer function; the inversion can have a significant effect on data results, and more accurately reflects the actual system behavior.

The inversion code was originally developed by Dr. José Moran for TDMA measurements of particle samples from the outlet of an electrospray precipitator (ESP) and was adapted for use with this experiment [37]. The inversion takes the particle size distribution function from the OPS (in a specific size bin) and raw charge state, as determined above, and considers the DMA transfer function and DMA penetration efficiency, enabling inference of the charge fraction, *f(z)*, for the diameter of interest. Equation 5 shows the mathematical relationship between the raw OPS reading, $\frac{\partial R(V, D_p)}{\partial D_p}$, when the DMA is set to a voltage V and data is collected for the size bin D_p between 0.3 and 10 μm. For all possible charge states,

$$\frac{\partial R(V, D_p)}{\partial D_p} = \sum_z \Omega\left(V, Z_p\right) T\left(D_p\right) f(z) \frac{\partial N}{\partial D_p} \qquad [5]$$

All parameters in Equation 5 are either known a priori, or measured, except for *f(z)*. The DMA transfer function, $\Omega\left(V, Z_p\right)$, accounts for the probability that a particle with a given electrical mobility Z_p, will be collected at the exit of the DMA when a voltage V is applied to its central rod. The DMA penetration efficiency is represented by $T(D_p)$, and the charge fraction, f(z) (for z > 0 elementary charges), is taken with respect to the particle size distribution $\frac{\partial N}{\partial D_p}$. This

relationship can be rewritten in matrix form, considering that $x(z|D_p) = f(z)\left[\frac{\partial N}{\partial D_p}\right]$, $b(V|D_p) = \frac{\partial R(V, D_p)}{\partial D_p}$, and $A(D_p, z) = \Omega(V, Z_p)T(D_p)$. Therefore:

$$\mathbf{b} = \mathbf{A}\mathbf{x} \qquad [6]$$

where $\mathbf{b} = \mathbb{R}^n, \mathbf{A} = \mathbb{R}^n \times \mathbb{R}^n,$ and $\mathbf{x} = \mathbb{R}^n$. The **b**, **A**, and **x** matrices are defined as follows:

$$\mathbf{b} = \begin{pmatrix} b(V_1|D_1) \\ \vdots \\ b(V_n|D_1) \end{pmatrix}$$

$$\mathbf{A} = \begin{pmatrix} A(V_1, z_1) & \cdots & A(V_1, z_n) \\ \vdots & \ddots & \vdots \\ A(V_n, z_1) & \cdots & A(V_n, z_n) \end{pmatrix}$$

$$\mathbf{x} = \begin{pmatrix} x(z_1|D_1) \\ \vdots \\ x(z_n|D_1) \end{pmatrix}$$

The resulting system of equations is an ill-posed Fredholm equation, which can be solved using a Tikhonov regularization with

$$\tilde{\boldsymbol{x}} = (\boldsymbol{A}^{\boldsymbol{t}}\boldsymbol{A} + \boldsymbol{\alpha}\boldsymbol{I})^{-\mathbf{1}}\boldsymbol{A}^{\boldsymbol{t}}\boldsymbol{b} \qquad [7]$$

This method can be attributed to Eq. 1.15, Vogel (2002); the exponent *t* refers to the transpose matrix, I is the n x n identity matrix, and α is the regularization parameter (between 0 and ∞) [38]. An optimum α must be selected to balance the effects of a low α (excessive noise, resulting in an oscillatory solution) and those of a high α (considerably reduced noise, but an over-smoothed solution). An L-curve criterion was used to determine the best regularization parameter for the inversion.

The L-curve is a method of evaluation that illustrates the "trade-off between the size of a regularized solution and its fit to the given data, as the regularization parameter varies" [39]. The plot of the L-curve is log-log, with the norm of the regularized solution, $\|x_a\|^2$, presented as a function of the corresponding residual norm, $\|Ax_a - b\|^2$ for the Fredholm equation, $Ax_a = b$. For each value of the regularized solution, the residual norm is determined and plotted; the data will often form an "L" shape around the optimal solution value. The L-curve criterion method generally provides a value that is more optimal than that produced from other methods of estimation [39].

The parameters which govern the deconvolution process can now be further defined: The DMA penetration efficiency was computed based on the parameterized results of Reineking & Porstendörfer (1986) [40], who stated the following equation:

$$T_l = 0.82\exp(-11.5u) + 0.1\exp(-70.0u) + 0.03\exp(-180.0u) + 0.02\exp(-340.0u).$$

The parameterized effective diffusion length, u, in the above equation is given by:

$$u = \frac{D_{ab} l_{eff}}{q_{sa}} \qquad [8]$$

where l_{eff} is the parameterized effective diffusion length, q_{sa} is the aerosol flow rate through the DMA, and D_{ab} is the particle diffusion coefficient [40]. However, for all particle sizes above approximately 50 nm, the penetration efficiency will be approximately 1.0, as was the case for the particle sizes tested here.

The diffusive broadened DMA transfer function is computed assuming balanced sheath and excess flows, using the expression below, which was developed by Stolzenburg and McMurry (2008) [41]:

$$\Omega(\tilde{z},\beta,\sigma) = \frac{\sigma}{\sqrt{2}\beta}\left[\epsilon\left(\frac{\tilde{z}-(1+\beta)}{\sqrt{2}\sigma}\right) + \epsilon\left(\frac{\tilde{z}-(1-\beta)}{\sqrt{2}\sigma}\right) - 2\epsilon\left(\frac{\tilde{z}-1}{\sqrt{2}\sigma}\right)\right. \quad [9]$$

where $\tilde{z} = \frac{Z_p}{Z_p^*}$ is the dimensionless mobility, Z_p is the particle mobility, Z_p^* is the centroid electrical mobility selected by the DMA, $\epsilon = x\text{erf}(x) + \left(\frac{\exp(-x^2)}{\sqrt{\pi}}\right)$, erf is the error function, and $\beta = \frac{q_{sa}}{q_{sh}}$. The parameter σ accounts for diffusional broadening of the transfer function; assuming plug flow, σ can be computed using the following equations from Hagwood (1999) [42]:

$$\gamma = \left(\frac{r_1}{r_2}\right)^2 \quad [10]$$

$$I = \frac{1}{2}(1+\gamma) \quad [11]$$

$$\kappa = \frac{lr_2}{r_2^2 - r_1^2} \quad [12]$$

$$G = \frac{4(1+\beta)^2}{1-\gamma}\left[I + \{2(1+\beta)\kappa\}^{-2}\right] \quad [13]$$

$$\sigma = \sqrt{\frac{2G\pi l d_{ab}}{q_{sh}}} \quad [14]$$

The inversion process was used on all data and provided information on the charge fraction, charge state distribution, and peak charge.

Summary of Methods

A series of DMA voltage scans were conducted using six different PSL solutions: 0.49, 0.8, 1.0, 1.6, 2.0, and 3.0 μm PSL sizes. For each PSL size, a unipolar ionizer was set to a fixed voltage and current; currents of 9, 10, and 12 μA were tested. After passing through the DMA, number concentration distributions were collected as a function of particle optical diameter, as measured by an OPS. Since each aerosol contained monodisperse particles, data were extracted from a single OPS size channel and used to determine particle concentration as a function of DMA voltage. Basic calculations were performed to determine the particle charge state associated with each DMA voltage, and the inversion process described above was used to convert the data to a charge distribution function for the known-size particles.

Both the "raw" charge distribution (determined from the voltages applied to the DMA and their corresponding charge states) and the processed, inverted results are presented in the Results and Discussion section.

Results and Discussion

Data was collected as described in the Methods section and manipulated to show the particle concentration as a function of applied DMA voltage and as a function of theoretical charge state, neglecting the effects of the DMA transfer function and penetration efficiency. To properly characterize the experimental system, the DMA and the unipolar ionizer were both tested and calibrated before starting data collection. Period calibration checks were also conducted to ensure the system continued to operate as desired. Following all experimental data collection, an inversion process was used as described in the above section to incorporate the effects of the DMA transfer function and penetration efficiency. These results were then compared with the initial "raw" data. The findings were also expanded beyond the aforementioned topics to theoretical experimental systems with different parameters; namely, systems with higher maximum DMA voltages and DMAs of different sizes, beyond the traditional "long DMA" lengths. Presentation and discussion of these results can be found below.

Calibration Results - DMA

Prior to commencing experimentation with large diameter, multiply charged particles, it was important to ensure the DMA was calibrated and providing results that agreed well with theory. A calibration test was conducted with a 200 nm PSL size-standard solution, using a setup like that shown in Figure 3. However, in place of the unipolar ionizer, a Po-210 source, acting as a neutralizer, was used. The neutralizer removed excess charges from the particles and applied a Boltzmann distribution of charges. The voltage applied to the DMA was stepped from 0 to 5 kV, and the particle concentration was measured in real-time using a Condensation Particle

Counter (CPC) operating at 0.4 lpm. This experimental setup, modified from that of Figure 3, is shown in Figure 5.

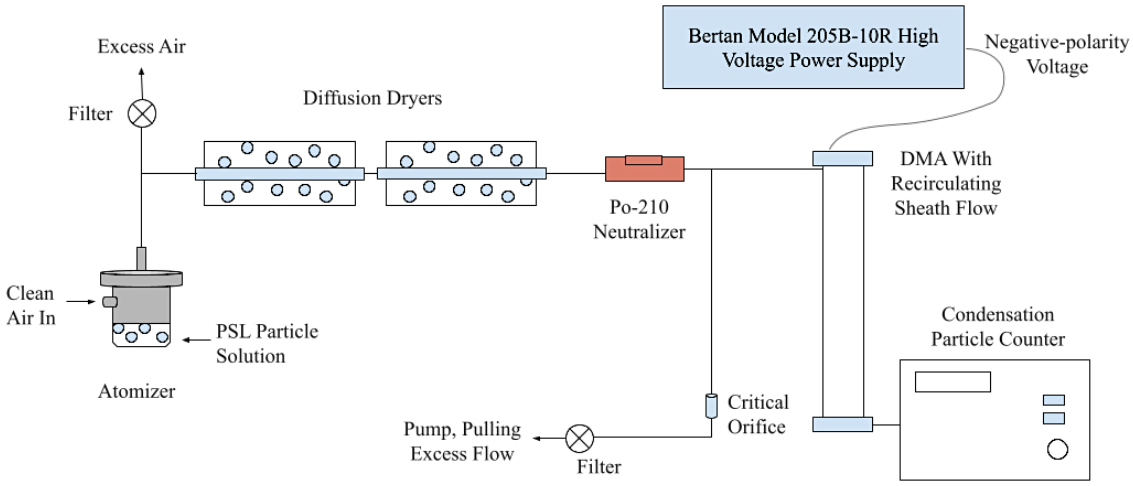

Figure 5. Experimental schematic for calibration testing. Particle are generated in an atomizer and conditioned using a series of diffusion driers. An equilibrium distribution of charge states (consisting primarily of 0, ± 1, and ± 2) is applied with a Po-210 neutralizer source. Particles are selected and analyzed using a combination of a DMA and a CPC.

A DMA voltage-particle concentration curve was generated using the CPC concentration data and the applied DMA voltages for each data point. Equations 1 and 2 were then used to convert the applied voltages to a "mobility diameter", in nanometers, which assumed a singly charged particle. A 200 nm particle was used for testing so that the singly charged peak could be observed, which is generally most consistent with theoretical calculations; a doubly charged peak should also be seen in this voltage range but was of secondary importance to the calibration.

Figure 6 shows the particle concentration as a function of (a) voltage applied to the DMA and (b) the associated mobility diameter.

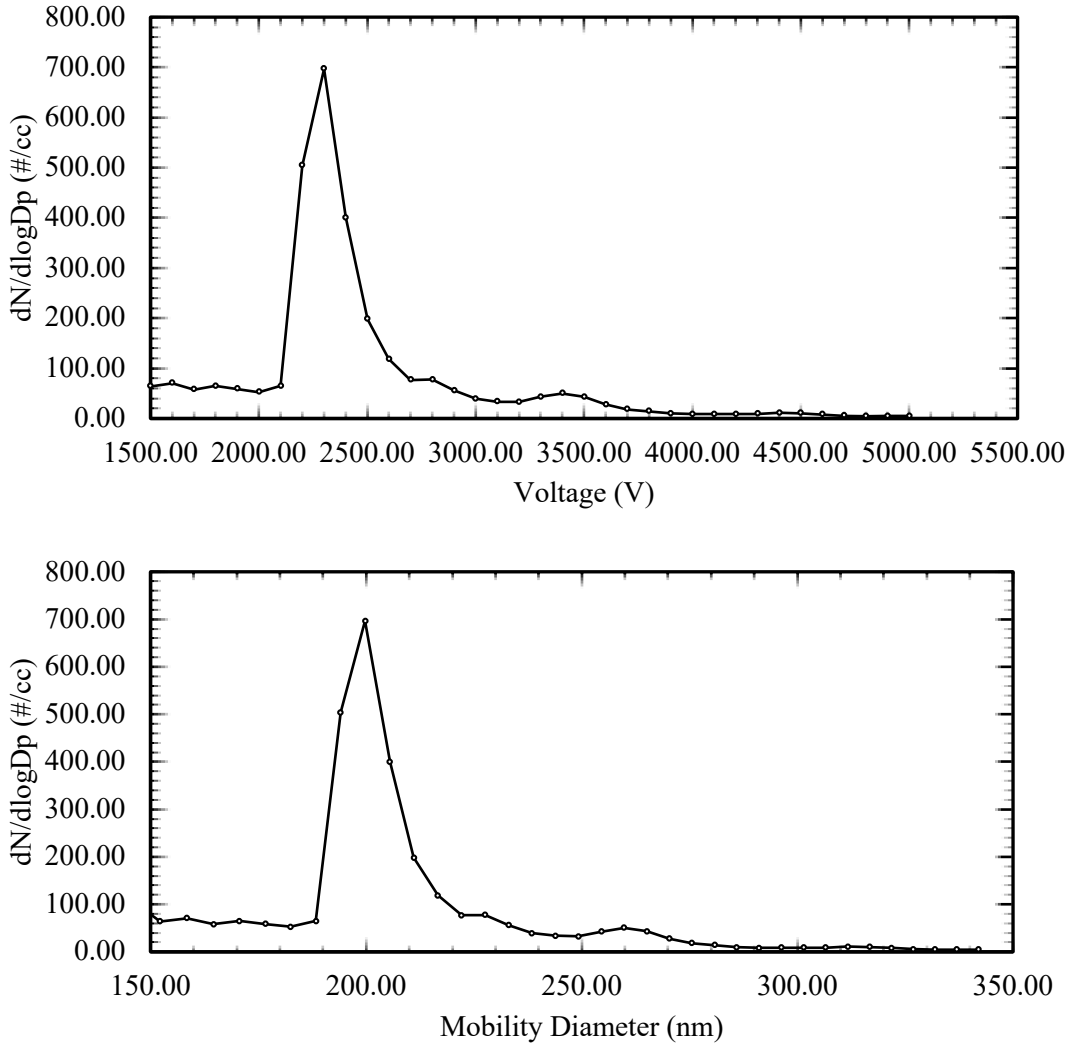

Figure 6. DMA calibration conducted with 200 nm PSL particles having a Boltzmann charge distribution, as applied by a Po-210 neutralizer. The (a) applied DMA voltage and (b) associated mobility diameter are shown. The singly charged, singlet peak can be observed at 2.3 kV, or a mobility diameter of 200 nm, as expected for calibration with a 200 nm PSL size standard solution. The dimer can also be observed at approximately 3.4 kV, or a mobility diameter of 260 nm.

A clear peak can be observed in Figure 6a at approximately 2.3 kV. When the testing parameters, including this peak voltage, are used with Equation 1, an associated mobility diameter of 200 nm is determined, as shown in Figure 6b. Since a 200 nm monodispersed PSL solution was utilized and the primary charge state was expected to be +1, these results indicate an acceptable DMA calibration.

Calibration Results – Unipolar Ionizer

Characterization of the unipolar ionizer was completed to determine its voltage-current response. This was necessary to ensure ion generation would be consistent between different experimental tests, since with each combination of applied voltage and corresponding response current, it is possible to produce a different number of ions or ions with different charging capabilities. The focus of the calibration was determining the current value (in μA) of the ions exiting the ionizer when a given voltage was applied. The voltage-current curve was constructed by stepping the ionizer voltage from the first onset of current response (as measured by an analog ammeter connecting the "ion outlet" of the ionizer to earth ground) up to the first indication of sparking behavior, in increments of 25 volts. A data point was taken when a new unit current state was achieved (for example, when the current value increased from 8 to 9 μA). This approach was meant to minimize measurement error associated with the relatively low resolution of the analog ammeter. At an applied ionizer voltage below 4.95 kV, there was no response current, and above an applied voltage of 6.18 kV, the ionizer began to exhibit sparking behavior, at which point data collection was suspended. Figure 7 shows the voltage-current curve for the ionizer, with supply voltage bounds of approximately 5 to 6 kV resulting in a range of currents from 3 to 14 μA.

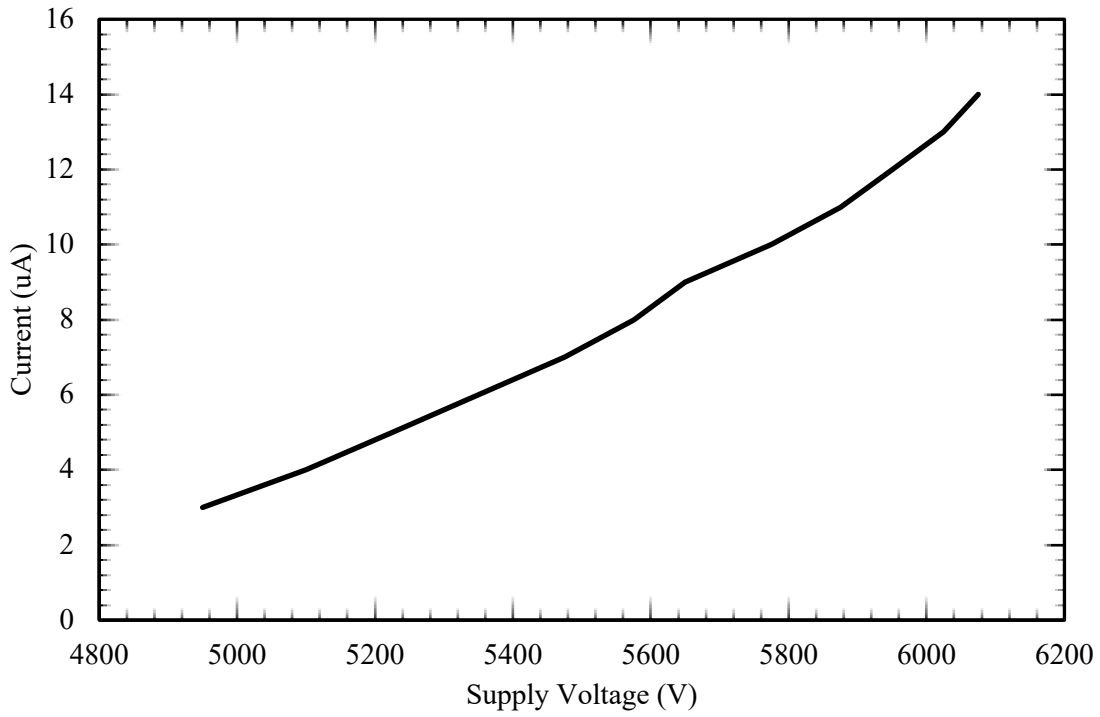

Figure 7. Unipolar ionizer current as a function of supply voltage. Consistent current behavior was observed between applied voltage of 5 and 6 kV, with resulting currents of 3 to 14 µA. Below 4.95 kV, there was no discernable ionizer current, while beginning at 6.18 kV, sparking began to occur. The current was measured every 25 volts, with data points recorded each time the current increased to the next unit value.

The voltage-current response curve for the ionizer was utilized throughout experimental testing, with applied voltages of 5.65, 5.84, and 5.975 kV corresponding to the three ionizer currents used in testing: 9, 10, and 12 µA, respectively.

Experimental Results – Non-inverted Data

For each of the tested PSL particle sizes (0.49, 0.8, 1.0, 1.6, 2.0, and 3.0 µm), three sets of unique particle number concentration data were generated, corresponding to the three tested ionizer currents (9, 10, and 12 µA).

Note that this non-inverted, or "raw" data does not consider the effects of the DMA transfer function, which will have a noticeable effect on results. The number concentration distributions were later used to determine associated charge distributions, which are shown following the concentration results. Both datasets were important tools for the inversion process, as they were used as a benchmark for the reliability and quality of a given inversion. It should be noted that the results for particles of larger diameter, particularly the 1.6, 2.0, and 3.0 particles, had significantly more error than the smaller tested particles due to the increasing width of the DMA transfer function with increasing particle size. The smaller particles were therefore more readily used as a comparison point to assess the validity of the inversion; this is discussed further in "Experimental Results – Inverted Data".

The concentration values are as exported from the OPS for the selected particle size bin (units of dN/dDp, or #/cc*μm). The particle size bins on the OPS were set to be as narrow as possible, to improve data resolution, and are as follows: 0.49 μm PSL: bin from 0.48 to 0.50 μm; 0.80 μm PSL: bin from 0.78 to 0.82 μm; 1.0 μm PSL: 0.9 to 1.1 μm; 1.6 μm PSL: 1.5 to 1.7 μm; 2.0 μm PSL: 1.9 μm to 2.1 μm; and 3.0 μm PSL: 2.75 to 3.25 μm. The DMA voltages applied for each data point were recorded during testing and later associated with the corresponding particle concentration data. Each data point shown in the results below is an average of at least two original data points measured by the OPS, for a given applied DMA voltage. Figures 8, 9, and 10 show the raw concentration data for 9, 10, and 12 μA ionizer currents, respectively, as a function of the voltage applied to the DMA.

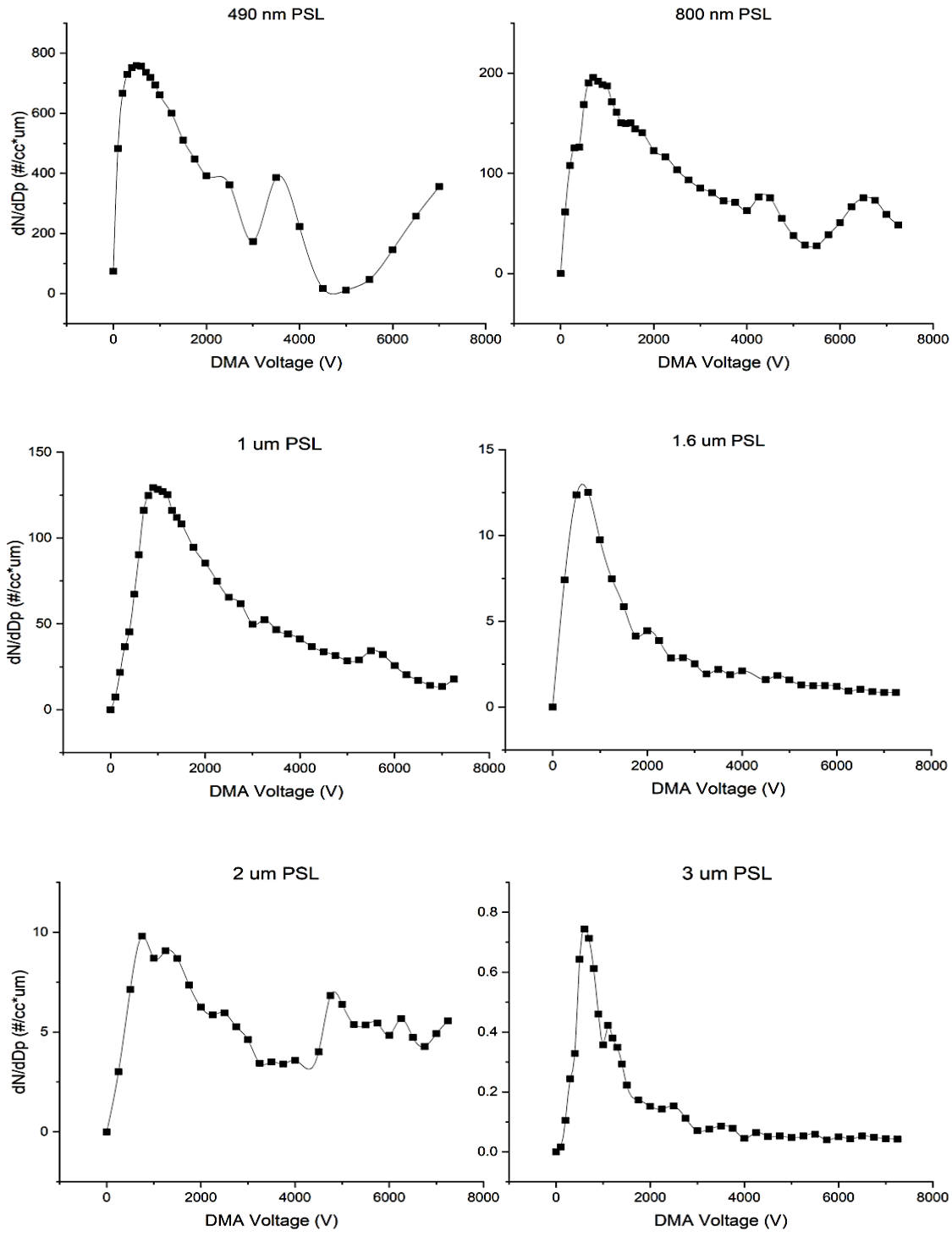

Figure 8. Raw number concentration curves as a function of voltage applied to the DMA, for ionizer operating at a current of 9 µA. These plots show the "raw" data, or the non-inverted dataset, which does not include the effects of the DMA transfer function.

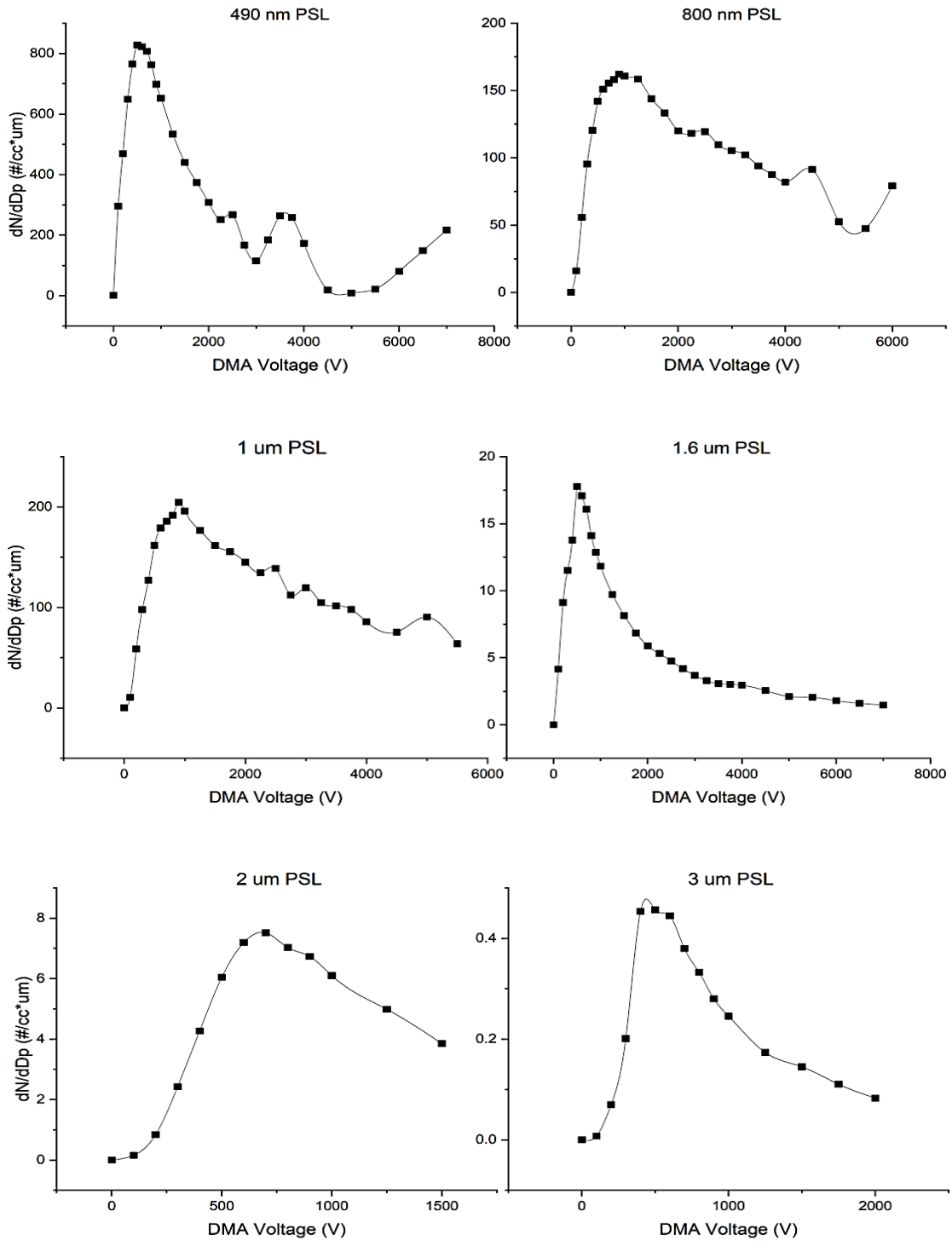

Figure 9. Raw number concentration curves as a function of voltage applied to the DMA, for ionizer operating at a current of 10 µA. These plots show the "raw" data, or the non-inverted dataset, which does not include the effects of the DMA transfer function.

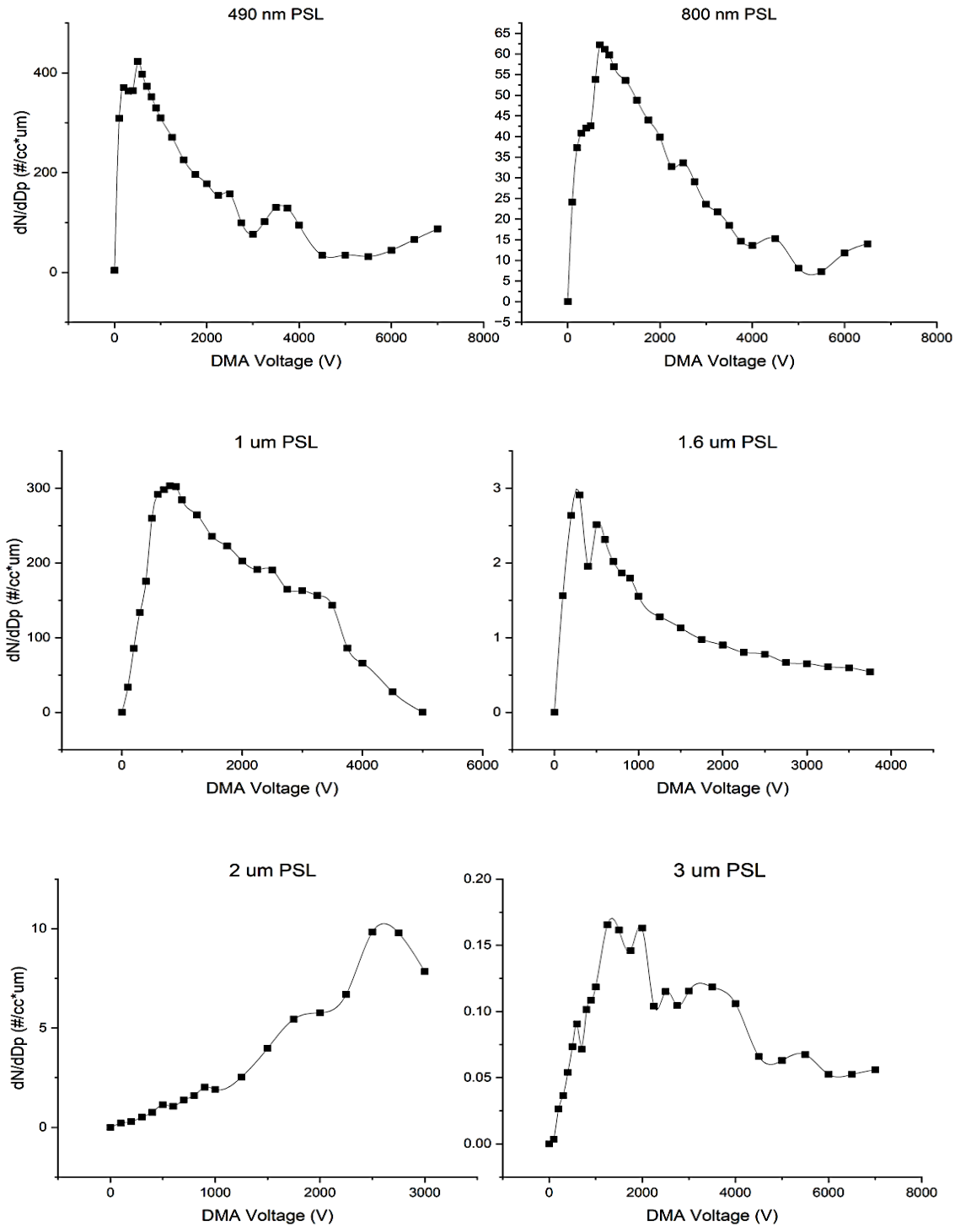

Figure 10. Raw number concentration curves as a function of voltage applied to the DMA, for ionizer operating at a current of 12 µA. These plots show the "raw" data, or the non-inverted dataset, which does not include the effects of the DMA transfer function.

For each of the plots shown in Figures 8-10, primary peaks are observable at or below applied DMA voltages of 2 kV; since the charge state is roughly proportional to the inverse of voltage, this indicates that most particles appear around the higher range of achievable charge states. There is a general trend that with increasing particle size, the voltage at which the primary peak is observed tends to decrease, and with increasing ionizer current, the "peak" voltage tends to decrease for the same particle size. This was not universally true, however, and possible causes or implications will be discussed further in subsequent sections. As the tested particle size and the ionizer current were both increased, particle losses significantly increased, which can be attributed to both gravitational settling and electrostatic losses.

From the applied DMA voltages used to generate the plots in Figures 8-10, the charge state associated with a given DMA voltage can be determined. This process is done using the particle electrical mobility, as shown in Equations 1 and 2. Since monodisperse PSL solutions were used, the particle diameter is known, and the charge state can be directly calculated with Equation 4.

It should be noted that this "raw" inversion of the charge state does not account for the DMA transfer function, which cannot be neglected and will have a noticeable impact on the results of inversion shown subsequently. The raw inversion was rather used as a benchmark for comparison between different ionizer currents results. Some of the results were also used in conjunction with the inverted results presented in a later section. Determining the charge state of the measured particles provides a correlation to previous literature results, particularly for submicrometer particle sizes, allowing for a theoretical comparison of previously measured electrical mobility and charge state results.

As was done for Figures 8-10, above, three sets of particle number concentration data were generated, corresponding to the three tested ionizer currents, and a unique charge state distribution was associated with each of the six tested PSL particle sizes. Figures 11, 12, and 13 show the particle number concentration data taken at ionizer currents of 9, 10, and 12 µA, respectively, as a function of the particle charge state. The particle charge state was inverted from the applied DMA voltage, as explained above. The concentration values are as exported from the OPS for the selected particle size bin and have units of dN/dDp, or #/cc*µm. The bounds of the OPS size bins were modified from the default, and are the same as were used for the number concentration distribution data shown in Figures 8-10.

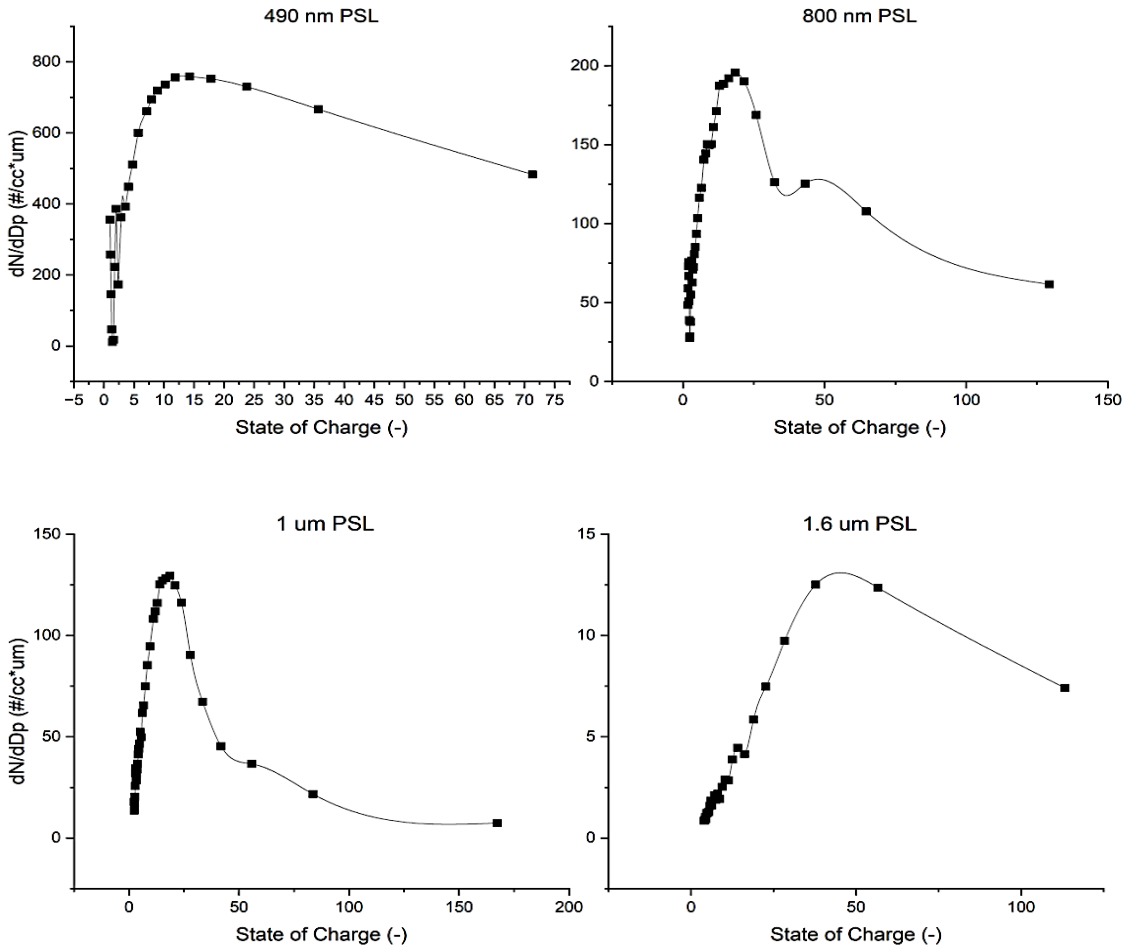

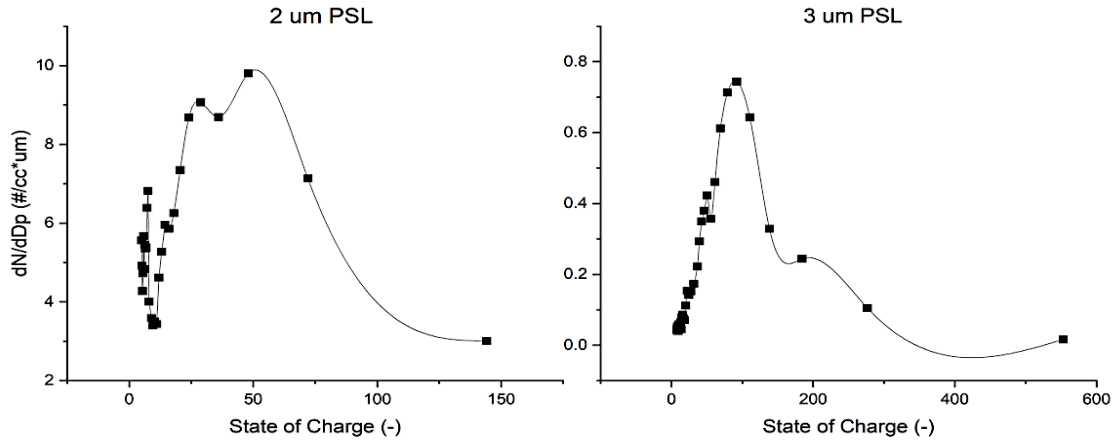

Figure 11. Raw number concentration curves as a function of calculated state of charge, for ionizer operating at a current of 9 μA. These plots show the "raw", or non-inverted dataset, which does not include the effects of the DMA transfer function.

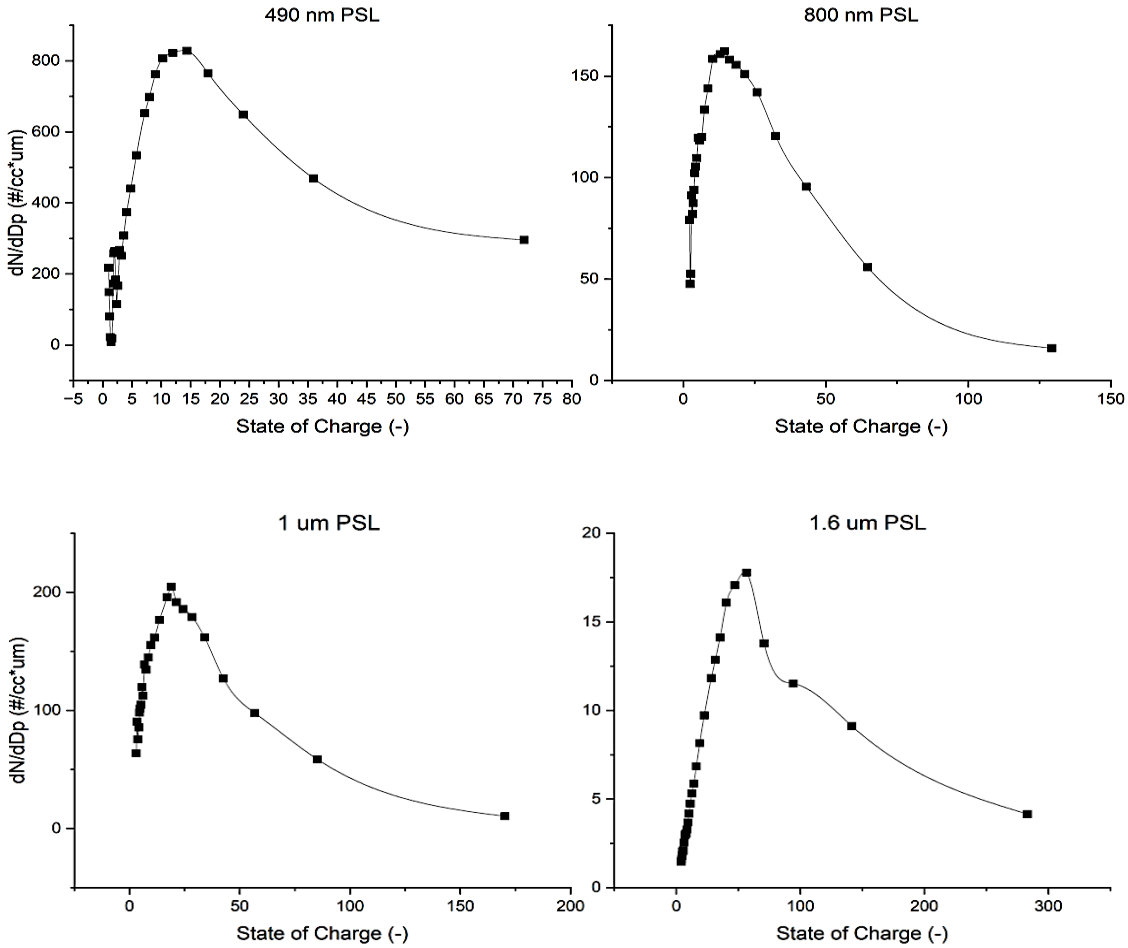

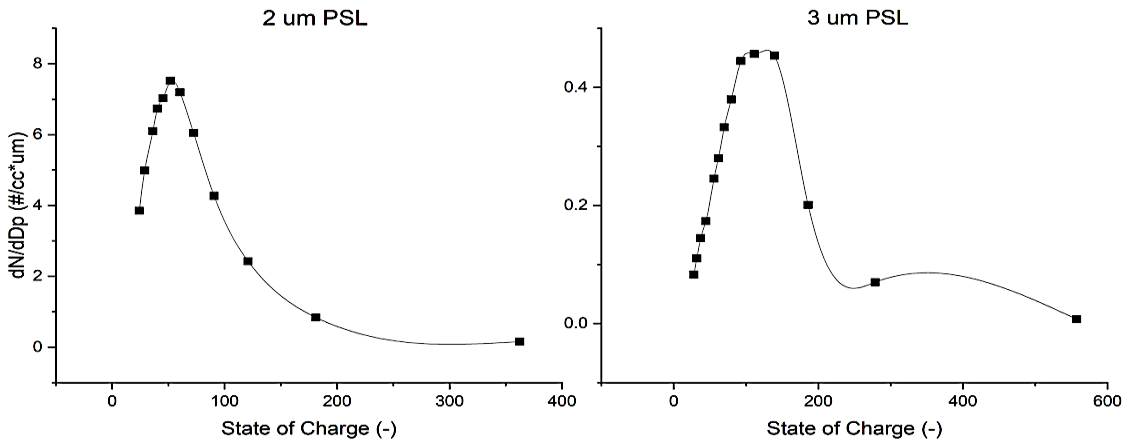

Figure 12. Raw number concentration curves as a function of calculated state of charge, for ionizer operating at a current of 10 µA. These plots show the "raw", or non-inverted dataset, which does not include the effects of the DMA transfer function.

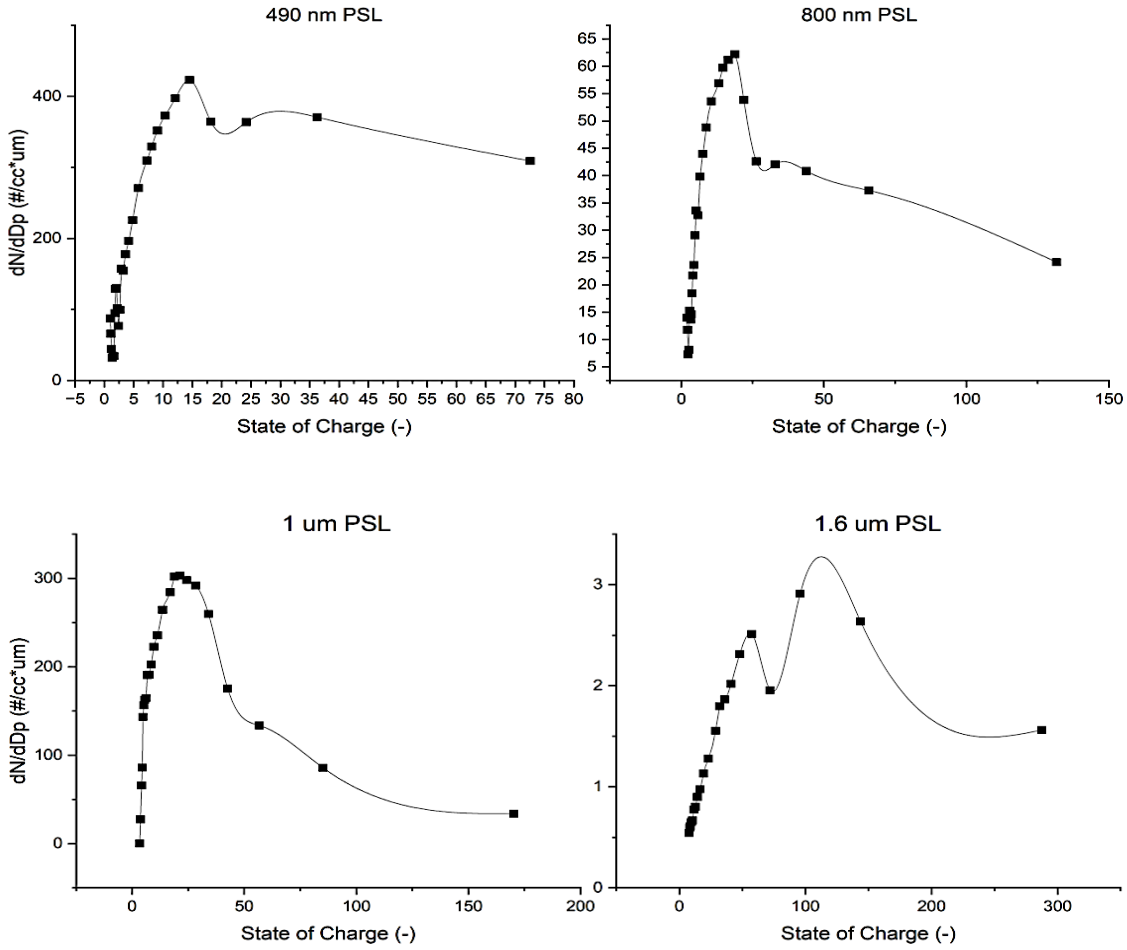

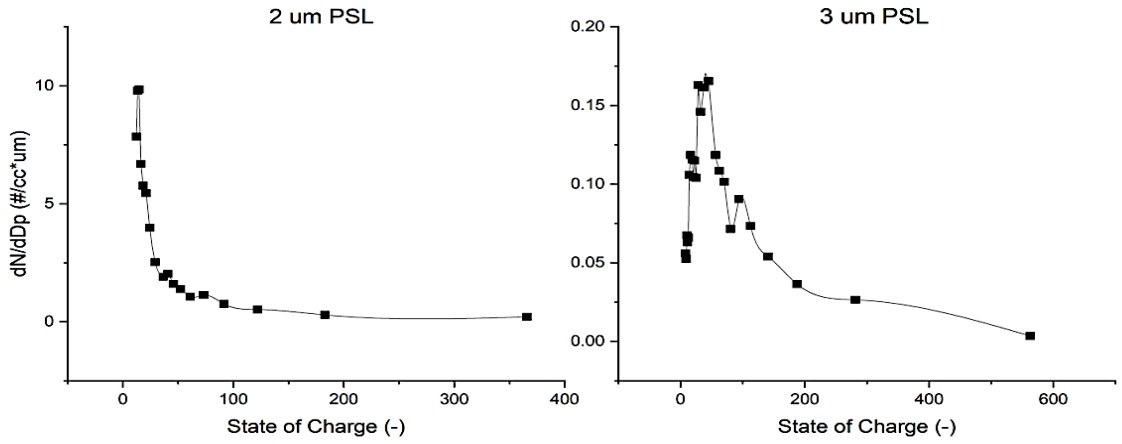

Figure 13. Raw number concentration curves as a function of calculated state of charge, for ionizer operating at a current of 12 μA. These plots show the "raw", or non-inverted dataset, which does not include the effects of the DMA transfer function.

From the results shown in Figures 11 to 13, several trends in particle charge state can be identified. Namely, the state of charge tends to increase as a function of both the ionizer current setting and particle size, with higher states of charge more readily obtained for larger particles and when the ionizer is set to a higher current level.

For many of the results shown above, the primary peaks encompass several unit charge states. For most results in which a particle is only singly or doubly charged, a distribution taken as a function of DMA voltage would reveal one or two sharp peaks, as was shown in Figure 6. At higher charge states, such as those used in these tests, the individual charge states tend to "clump" together, forming a broader peak that encompasses several peak charge states. For the purposes of analysis, a single peak charge state, at which a maximum number concentration was obtained, was chosen and extracted from the results above. These peak charge states were used for quantitative analysis, presented in "Experimental Results – Peak Charge States".

Experimental Results – Inverted Data

The formal inversion process described in the Methods section was used to account for the effects of the DMA transfer function and particle penetration efficiencies in the charge distribution results. Charge state values determined purely mathematically from the non-inverted particle concentration data were used throughout testing as an indicator of data trends, but did not fully reflect the intricacies of the experimental system. While the smaller particle size results could be used as a relatively accurate benchmark reference for the quality of the inversion process, the same was not true for larger diameters, with an increasing disparity occurring between the "raw" and formally inverted results as the tested particle size was increased. For particle sizes larger than a diameter of 1.0 μm, the DMA transfer function began to have a significant impact on the charge state distribution results; therefore, the raw results at these larger particle sizes were not used as a benchmarking tool for the inversion process but remained helpful for assessing general data trends. An example of the DMA transfer function for each of the tested particle sizes is shown in Figure 14, with the DMA transfer function shown as a function of the unit state of charge. Note that Figure 14 is meant to merely illustrate how the transfer function would change with increasing particle size. The transfer function will also change depending on the DMA conditions, including applied voltage; here, it is shown at a fixed DMA voltage of 4 kV.

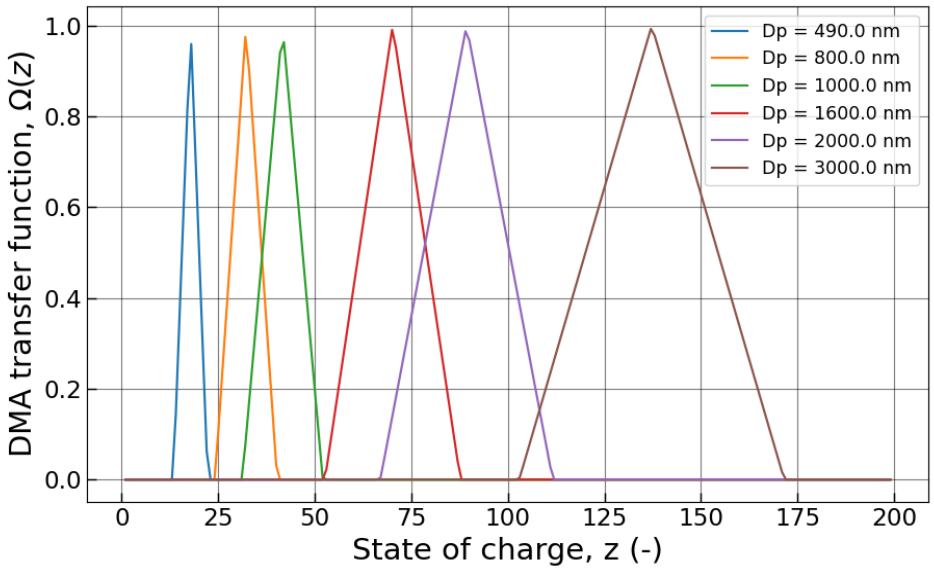

Figure 14. DMA transfer function, as determined for the six tested particle sizes. The transfer functions shown were found at a fixed voltage of 4 kV, and are meant to demonstrate the increasing effect of the transfer function with increasing particle diameter; however, they are not meant to be numerically representative, as the transfer function changes with system characteristics included applied DMA voltage.

As explained in the Methods section, the transfer function is the probability that a given particle will successfully pass through an electrostatic classifier such as a DMA [43]. The particle will have certain characteristics that allow it to traverse the classifier, including a set electrostatic mobility (which accounts for a combination of particle size and charge), and a given diffusion coefficient (related to the particle diameter). A variety of expressions can be used for the transfer function, depending on whether the effects of diffusion, or gravity, among others, are considered. For this work, the Stolzenburg (2008) transfer function shown in Equation 9 and illustrated in Figure 14 was used throughout [41]. Further details can be found in the Methods section.

Figure 14 illustrates how the transfer function begins to significantly impact and even dominate the inversion process above 1.0 μm, with 3.0 μm particles having a transfer function width of nearly 75 states of charge for this example plot. The process used to determine the "raw" charge states obtained for each particle size (as shown in Figures 11-13) neglects the DMA transfer function width, considering only the "peaks" of the transfer functions illustrated in Figure 14. As the particle size increases and the transfer function widens, however, the effects of the transfer function become non-negligible and must be taken into consideration using an inversion process.

Another factor that was taken into consideration for the inversion process was the DMA particle penetration efficiency. The penetration efficiency is a size-dependent parameter related primarily to diffusional particle losses that occur at the entrance and exit of the DMA. However, for the particle sizes tested here, the penetration efficiency was approximately a constant value of 1 and was neglected, as the particles were larger than 50 nm.

While the DMA transfer function and penetration efficiency will account for most particle losses, they do not fully capture the effects of electrostatic deposition, which may begin to impact particles at or above 1 μm in diameter, especially those exposed to a higher ionizer current. Overall, accounting for both the DMA transfer function and penetration efficiencies was determined to be sufficient for an accurate inversion.

For the inversion process, an L-curve criterion was introduced to determine an optimal α, or regularization parameter, at each tested particle size. As shown in Figures 15-17 an "L-curve" associated with a large set of possible alpha values was assembled for each particle diameter and ionizer current.

For each test case, the solution value, x_α, and associated residual, $Ax_\alpha - b$, were determined, normalized, and plotted on a log-log scale. These points formed an "L" shape, with the optimal solution appearing at the "bend" in the "L". The points on the left side of the "L" tended to be oversmoothed, while those points appearing on the right side of the "L" tended to have excessive noise. The L-curve criterion is described further in the Methods section.

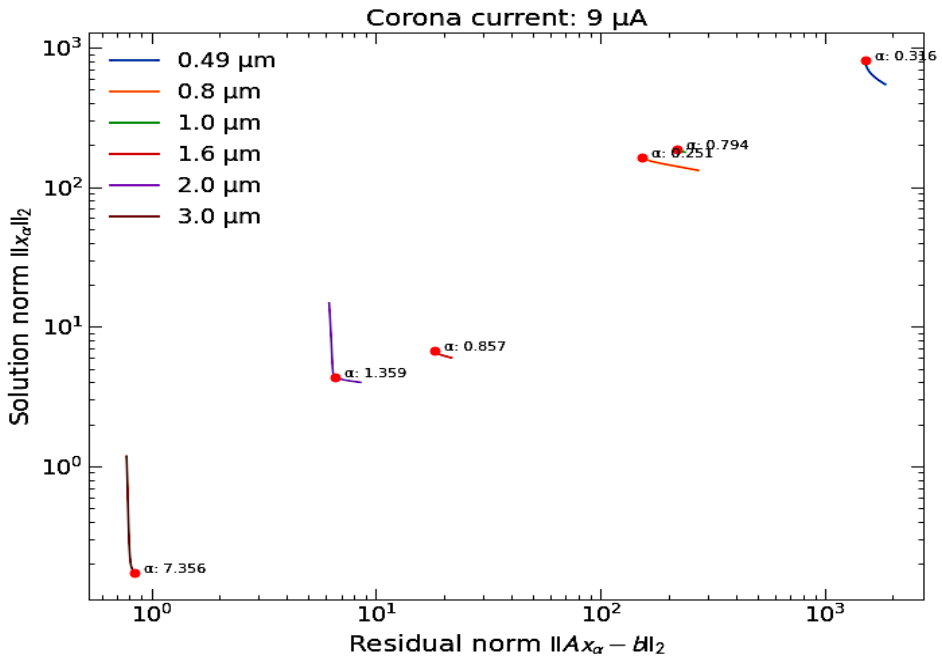

Figure 15. L-curve criterion for 9 µA ionizer, used to determine an optimal regularization parameter, α, for use with each particle size in the inversion process. The optimal solution value was determined by minimizing the residual of the inversion matrix problem, Ax-b.

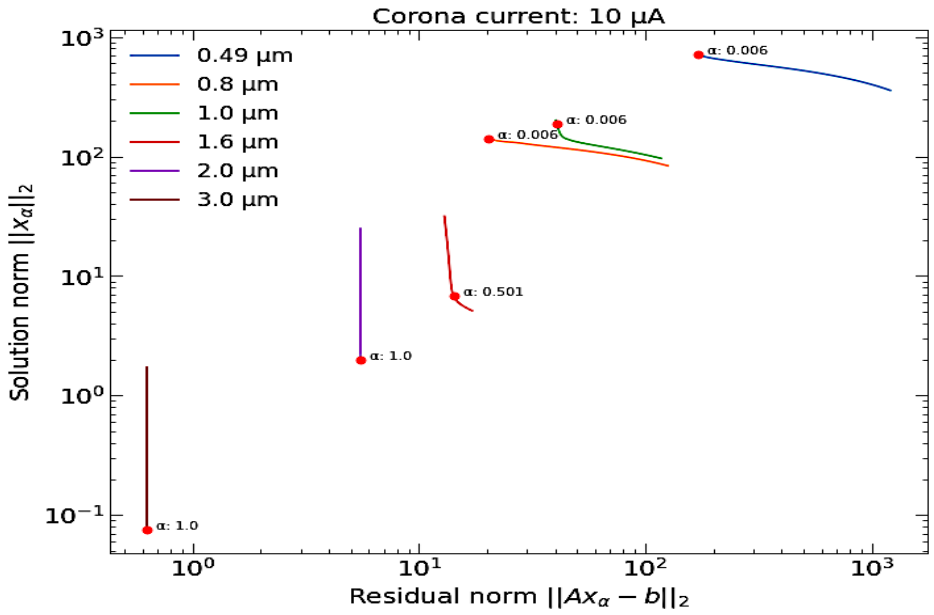

Figure 16. L-curve criterion for 10 µA ionizer, used to determine an optimal regularization parameter, α, for use with each particle size in the inversion process. The optimal solution value was determined by minimizing the residual of the inversion matrix problem, Ax-b.

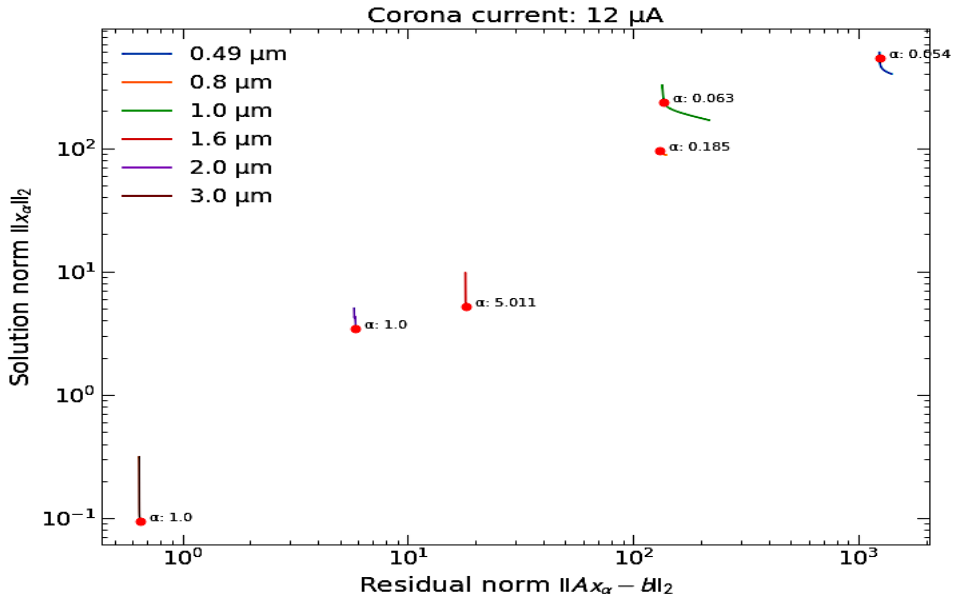

Figure 17. L-curve criterion for 12 µA ionizer, used to determine an optimal regularization parameter, α, for use with each particle size in the inversion process. The optimal solution value was determined by minimizing the residual of the inversion matrix problem, Ax-b.

Once an optimal regularization parameter was selected for each tested particle size, the formal charge state inversion routine was used on the raw data that was presented in Figures 8-10. The inverted data included the effects of the DMA transfer function, providing a more robust and accurate understanding of the experimental results.

One of the parameters of interest for the inverted data was the particle charge fraction. The charge fraction is defined as the fraction of particles carrying a "specific number of charges", and represents "the ratio of the charge distribution to the size distribution" [44, 45]. The charge fraction for aerosols is typically determined using Tandem DMA (TDMA) analysis methods but was also possible to obtain using the setup described in this paper.

The charge fraction can be explained by first considering an equilibrium charge distribution, which will be primarily composed of neutrally or singly charged particles of either negative or positive polarity. A few other particles will be doubly charged, with either polarity. When these particles then combine with the ions produced in the ionizers through random collisions, the probability to have a higher number of charges increases. Similarly, with a higher corona current in the ionizer, more ions are produced, and there is a greater probability for a higher charge state. As described here, the charge distribution is dependent on charging conditions and particle characteristics, and can often be theoretically predicted using Fuch's charging theories or the more recent work of Gopalakrishnan and coworkers [46]. These theories, however, are not well characterized for particles larger than 1 μm in diameter.

Figures 18 through 20, below, show a calculated charge fraction distribution as a function of the number of elementary charges, for each of the six tested particle sizes with the ionizer set to 9, 10, and 12 μA in Figures 18, 19, and 20, respectively.

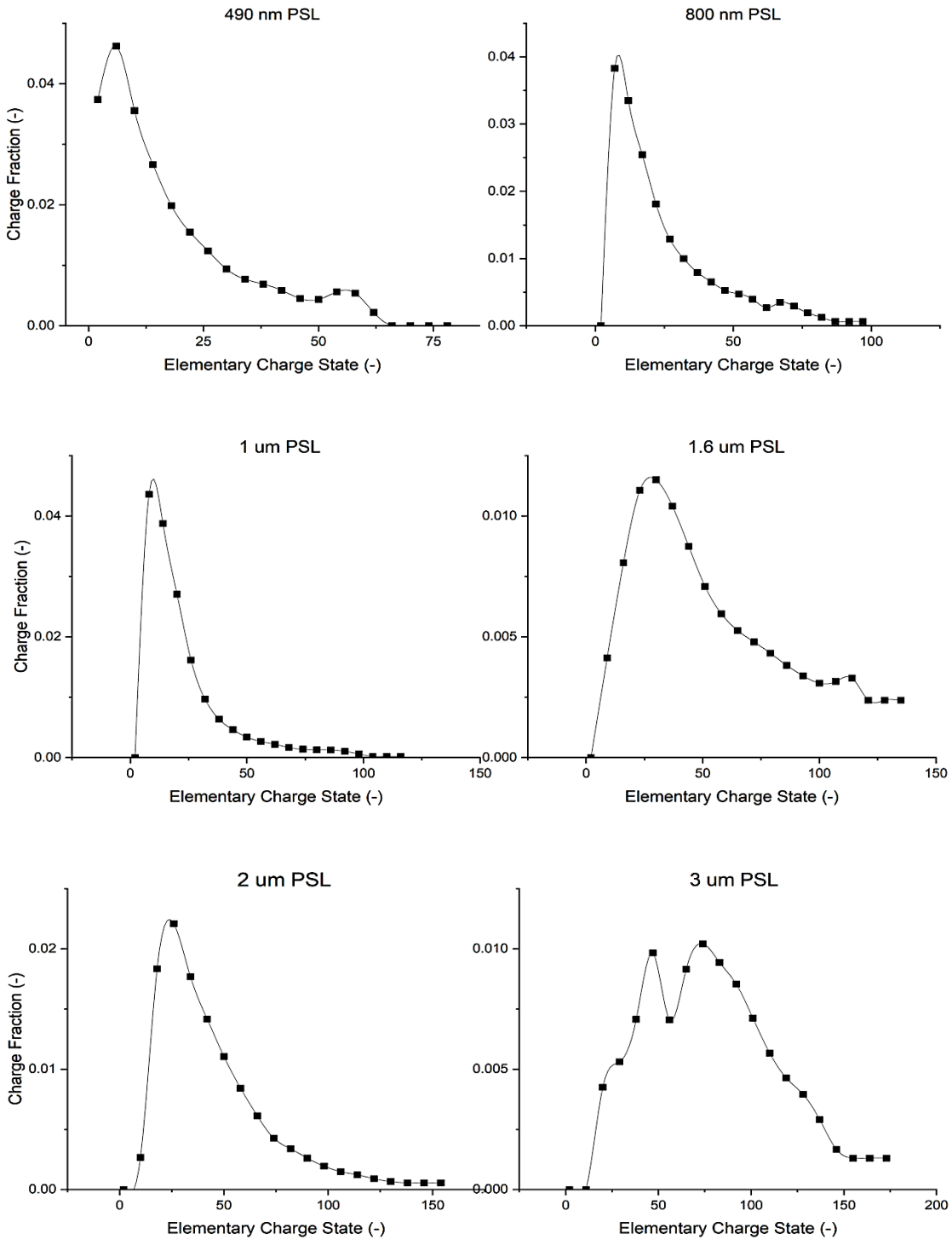

Figure 18. Inverted charge fraction curves as a function of elementary charge state, for ionizer operating at a current of 9 μA.

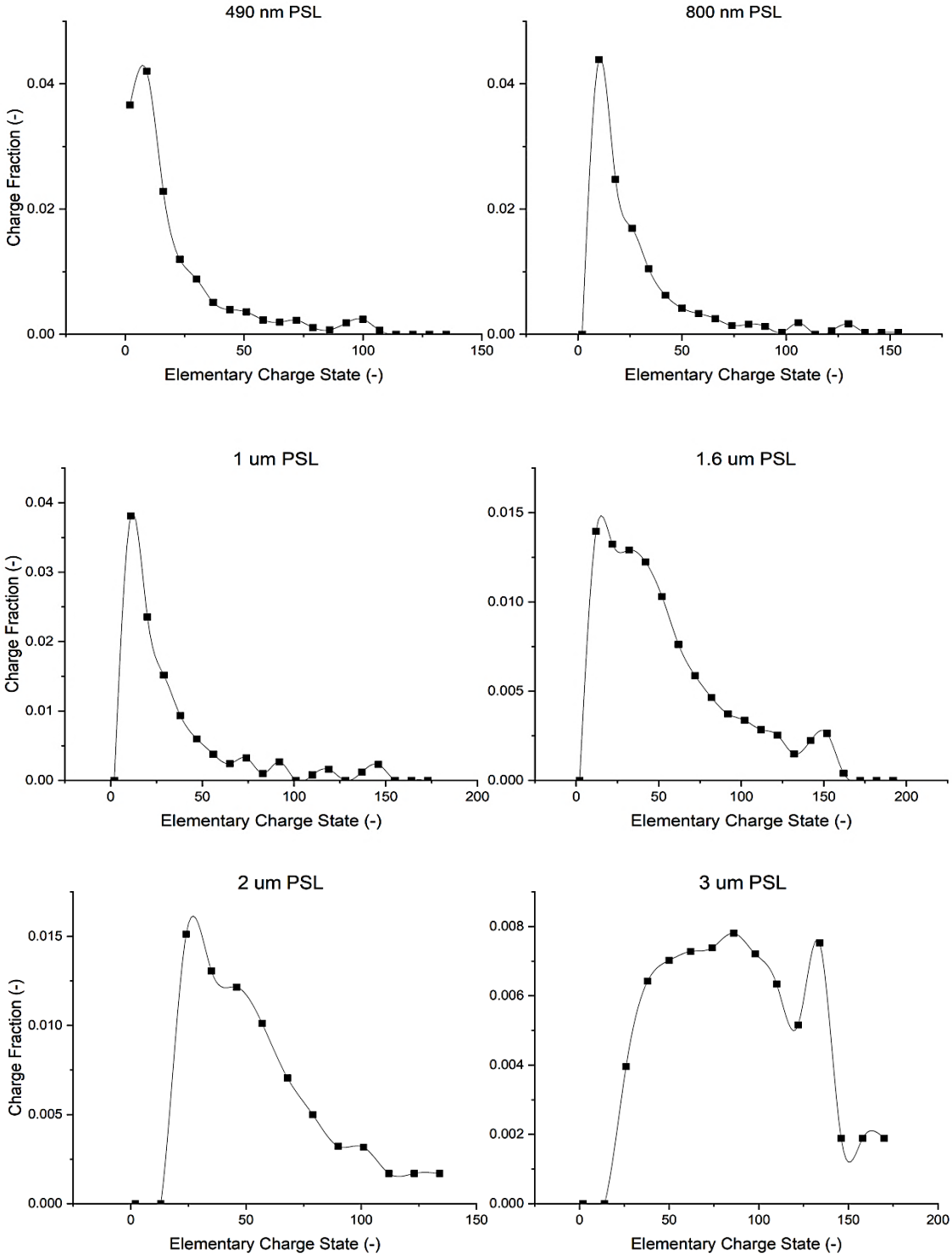

Figure 19. Inverted charge fraction curves as a function of elementary charge state, for ionizer operating at a current of 10 μA.

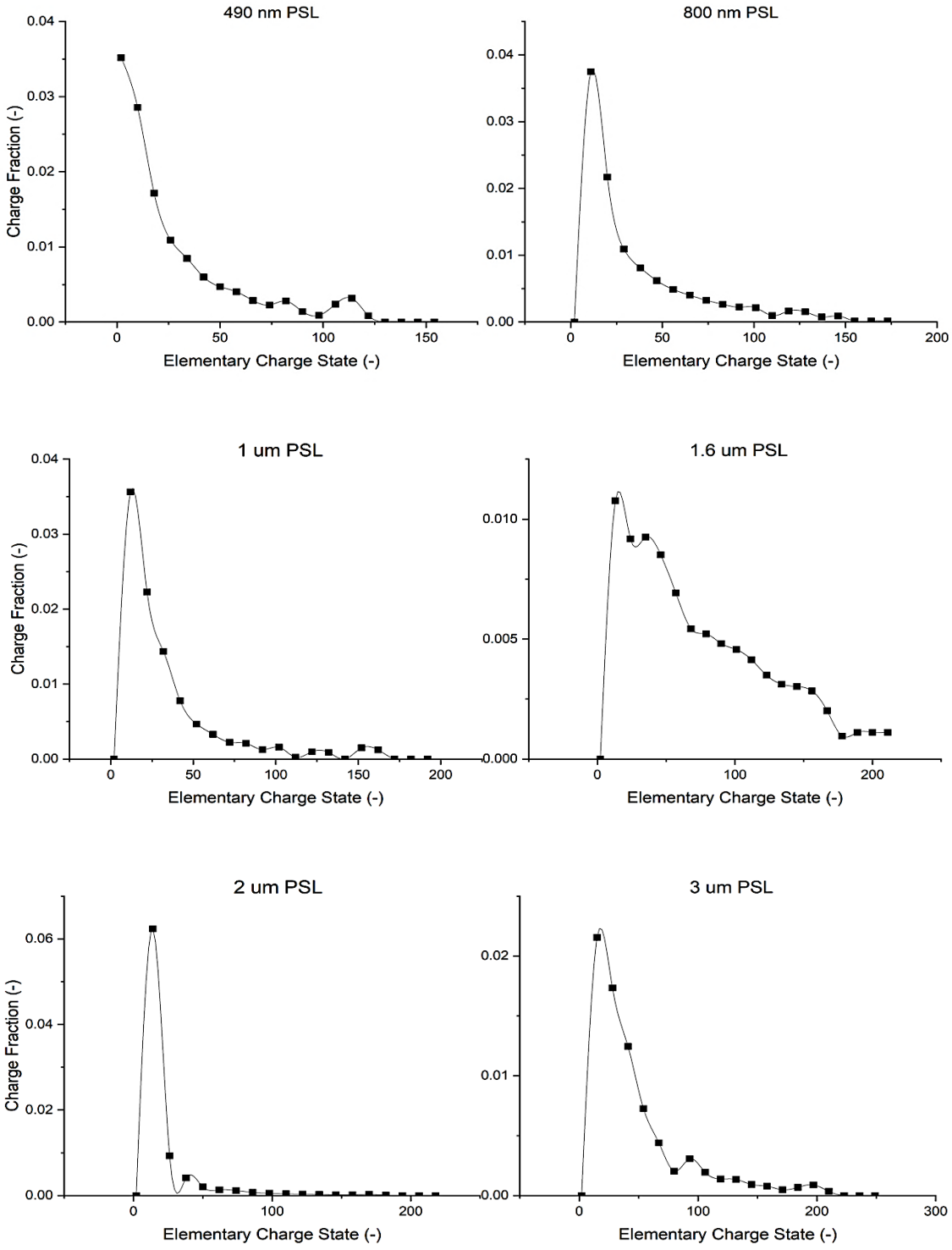

Figure 20. Inverted charge fraction curves as a function of elementary charge state, for ionizer operating at a current of 12 μA.

Figure 21 shows a combined non-inverted ("raw") and inverted charge fraction for 2 µm particles at the three ionizer currents.

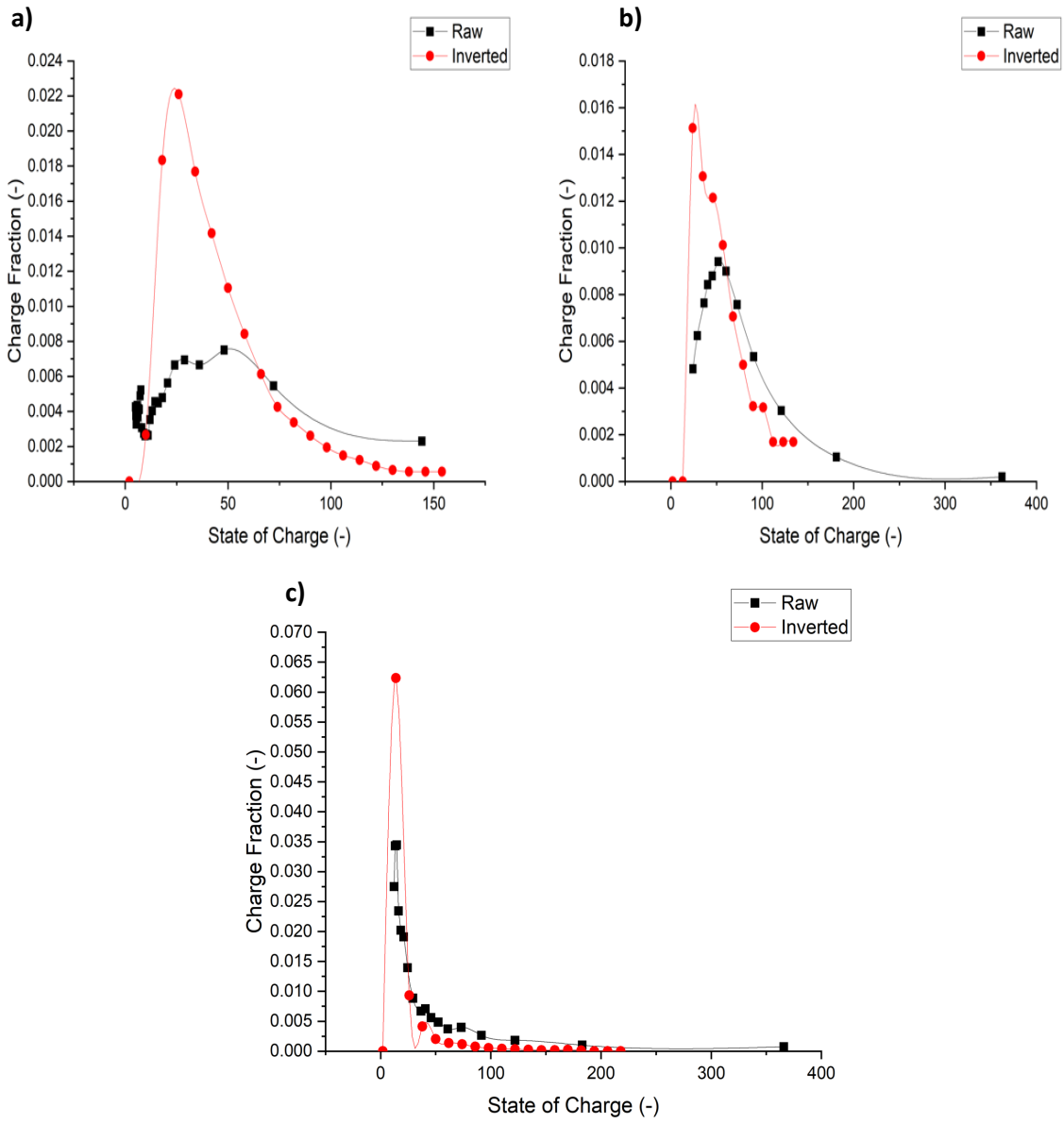

Figure 21. Charge fraction for 2 µm particles, showing both non-inverted ("raw," represented by square symbols) and inverted (represented by circular symbols) data, for an ionizer current of a) 9 µA, b) 10 µA, and c) 12 µA.

The results observed here confirm the expected trend of an increasing number of charge states associated with an increasing particle size and ionizer corona current. This is most clearly illustrated in Figure 18, in which the charge state at which the greatest charge fraction occurs can be seen to increase with particle size. The largest charge state obtainable at a charge fraction greater than zero also increases with the same variables, as illustrated very clearly for the 1.6 μm results between Figures 18-20. For most of the results, the charge state at which a maximum charge fraction was obtained tended to fall between +25 to +50 elementary charge states.

Figure 21 further illustrates the shift in charge state between the "raw" and inverted data, showing the charge fraction as calculated for non-inverted, 2 μm data. This is most clearly shown in Figure 21b, the 10 μA data, where the curve is observed to shift towards the left, or lower charge states, for the inverted data. The charge fraction values, by contrast, were observed to increase overall for the same states of charge.

One notable aspect of these results is the shape of the curves, which would typically take the shape of a Gaussian distribution. These results, however, tend to take a right-skewed, or positively skewed, shape, giving them a long tail towards the right side of the distribution. The non-uniformity of the distribution can be attributed to the effects of both charging and electrostatic deposition. As explained above, the particles tend to have an equilibrium distribution of charges prior to interaction with ions produced through the ionizer; while they are then able to achieve higher charge states, there is a limit to the number of charges which can be passed to the particles purely through ion collisions, as Coulombic repulsion decreases the charging rate for highly charged particles. The particles themselves would be capable of

carrying many more unit charges, limited only by the Rayleigh charging limit, but the charging method used here does not allow for sufficient collisions to reach this limit. Additionally, for particles that may achieve higher charge states than those measured here, it is likely they begin to experience electrostatic deposition in either the ionizer or the DMA. Both factors cause the charge fraction to taper off for higher charge state values, which in turn causes the observed positively skewed distribution.

The non-symmetrical curve shape observed here is further confirmed by results previously obtained by Järvinen et al. (2017), which showed similarly skewed charge fraction distributions [23]. For that investigation, however, an inversion routine was not used to account for the DMA transfer function; as shown above, the inversion will tend to shift particle charge states even lower for a given data point. The charging method used in the work of Järvinen also differed, with an Electrical Low-Pressure Impactor (ELPI) charger used for particle charging. Due to the high currents achievable with the ELPI, the particles tended to have much higher charge states overall, preventing a direct comparison of the charge fraction distributions, even for non-inverted data.

Emets, Kascheev, and Poluektov (1991) and Forsyth, Liu, and Romay (1998), who employed similar experimental procedures to what is shown in the Methods section, both used bipolar ionization, which prevents a direct comparison of data [28-30]. For some of their experiments, the charge distribution was established using a neutralizer, which will apply a Boltzmann distribution having many fewer unit charges than would be applied by an ionizer; this further prevents comparative analysis. Biermann and Bergman (1984) also conducted their experimentation with a similar testing setup; however, for the tested particle sizes that are

comparable to those tested in this investigation, there is insufficient numerical data available to allow for a direct comparison [28]. As mentioned previously, all three do not offer a data inversion that would account for the DMA transfer function.

Experimental Results – Peak Charge States

For each data curve, a peak charge state, or charge state at which a peak concentration was obtained, could generally be identified. The peak charge state for each of the non-inverted data sets was identified directly from the calculated charge states. For those instances in which a peak encompassed several voltages and their associated charge states, or when a non-integer charge state was obtained, the charge state was rounded to the next highest unit value. Since data was not measured continuously, the peak charge state values are approximate; additional experimental analysis or interpolation would be necessary to robustly determine a peak charge state. However, for the purpose of assessing general trends and comparing with inverted data, this method provided results of an acceptable quality.

A similar, but more thorough, analysis approach was used to assess the peak charge states of the inverted data. For each plot of charge fraction as a function of charge state, a spline was fitted to the data, and interpolation along the spline was used to determine the "peak" charge state value or the charge state at which a maximum charge fraction was obtained. Since data was not taken continuously, this interpolation was used to provide a peak charge state with as much accuracy as possible.

The peak charge state is presented in Figures 22-27 as a function of the current value of the ionizer. Figures 22-24 show the results for the non-inverted, or raw, data, for ionizer currents

of 9, 10, and 12 µA, respectively. Figures 25-27 show a comparison of the inverted and raw data results for the same ionizer current values.

Non-inverted ("Raw") Peak Charge States

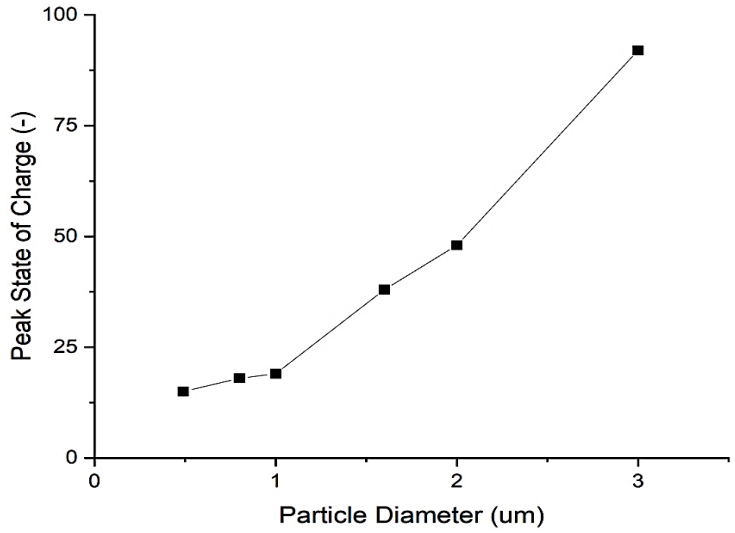

Figure 22. Non-inverted peak charge as a function of size for ionizer operating at a current of 9 µA.

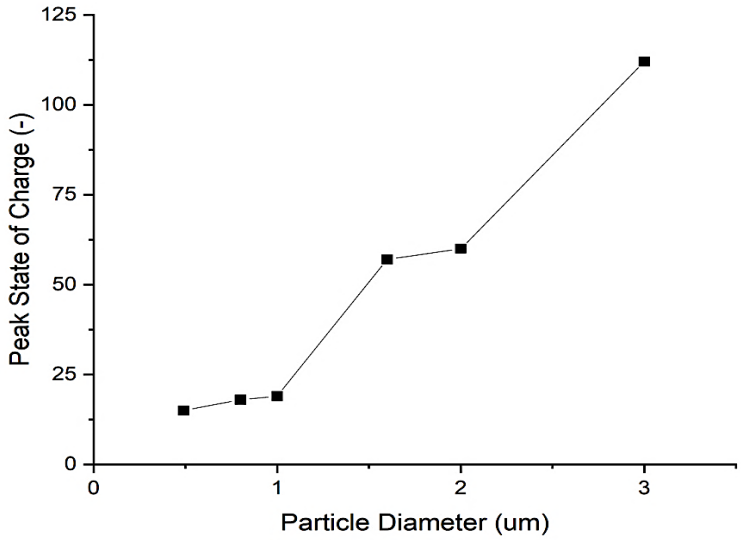

Figure 23. Non-inverted peak charge as a function of size for ionizer operating at a current of 10 µA.

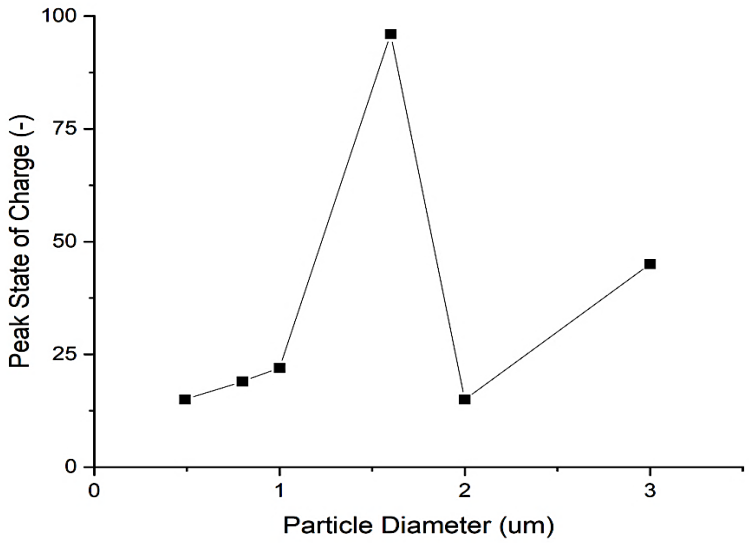

Figure 24. Non-inverted peak charge as a function of size for ionizer operating at a current of 12 µA.

Comparison of Non-Inverted and Inverted Peak Charge States

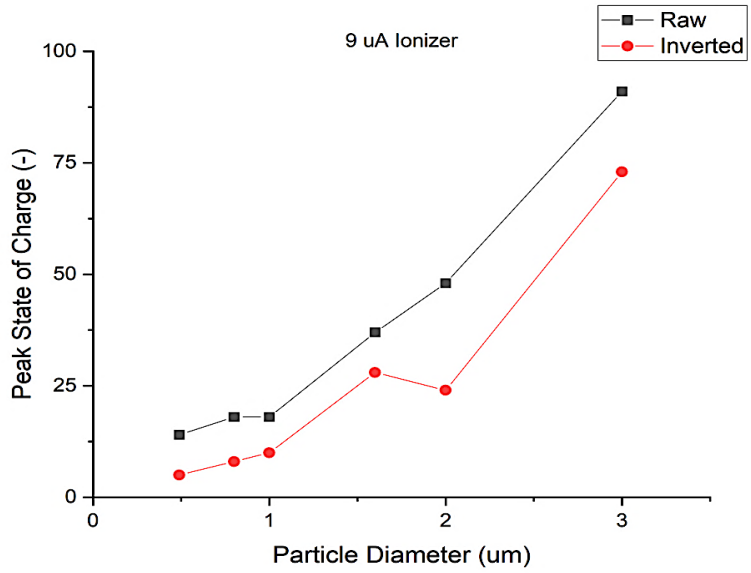

Figure 25. Non-inverted and inverted peak charge as a function of size for 9 µA ionizer. The peak charge state was determined using interpolation of the charge fraction distributions.

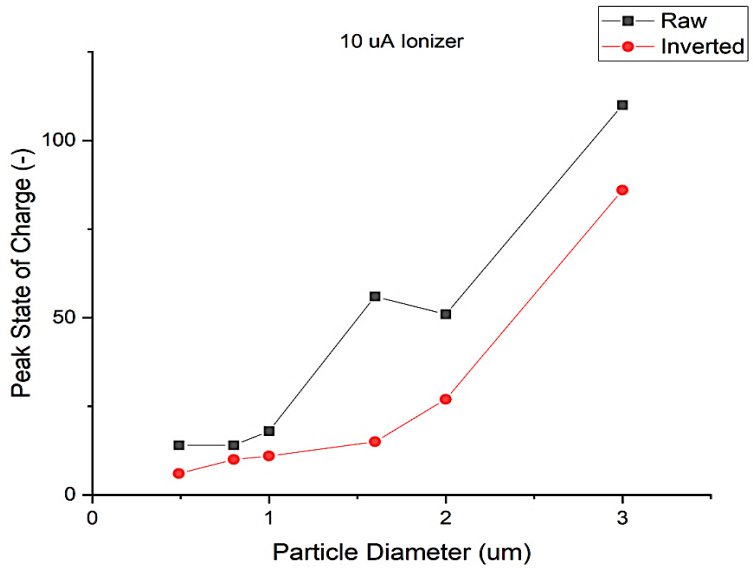

Figure 26. Non-inverted and inverted peak charge as a function of size for 10 µA ionizer. The peak charge state was determined using interpolation of the charge fraction distributions.

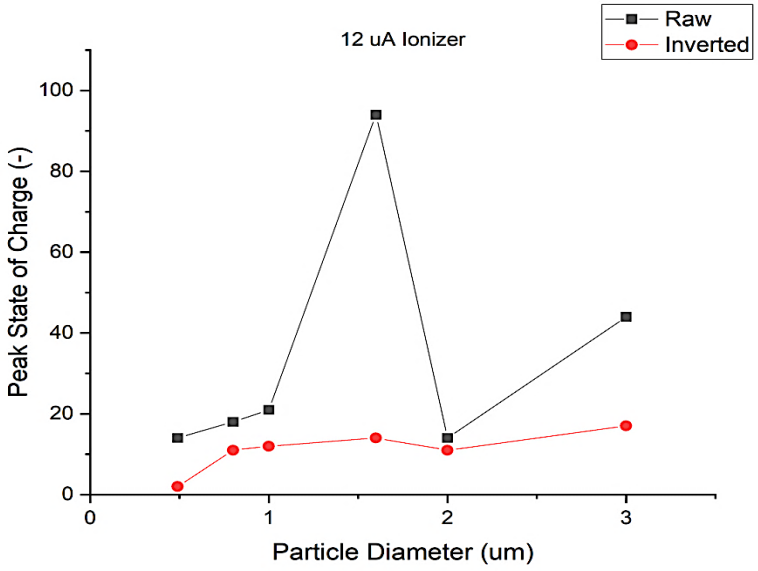

Figure 27. Non-inverted and inverted peak charge as a function of size for 12 µA ionizer. The peak charge state was determined using interpolation of the charge fraction distributions.

The non-inverted peak charge states shown in Figures 22-24 depict a clear trend in charge states as both the tested particle size and ionizer current level are increased. For the submicrometer particles, all the measured peak charge states fall around +15 to +20, with significant increases in the peak charge state for supermicrometer-sized particles. As the ionizer current was increased, the measured peak charge state was also observed to significantly increase for supermicrometer particles. For example, with 1.6 μm particles, peak charge states of approximately +40, +55, and +95 were observed with ionizer current levels of 9, 10, and 12 μA, respectively, indicating that additional ions are generated at higher ionization currents and that they have a noticeable impact on the peak charge states, increasing them substantially.

One notable exception to this trend was for the 2 and 3 μm particles at an ionizer current of 12 μA. A drop in peak charge state was observed between the 1.6 and 2 μm, with 1.6 μm particles having a state of +95, and 2 μm particles having only approximately +15. While the peak charge state did increase for 3 μm particles (state of approximately +45), it does not reach even the peak charge state achieved by 3 μm particles when the ionizer current was set to 9 μA, which was around +95. A plausible explanation for the disparity is increasing electrostatic losses associated with highly charged, larger particles. From the results shown in Figures 11-13, while there is a measurable concentration at higher charge states, they do not tend to be dominant in terms of measured particle concentration. As for the 2 and 3 μm results measured with an ionizer current of 12 μA, the lower concentrations observed at higher charge states can be explained by electrostatic losses. These losses may occur near the ionizer, where particles could impact on the walls of the "tee" tubing used to intersect particles and ions, or losses

could occur within the DMA, with deposition (on the walls, inlet, outlet, etc.) occurring more frequently for more highly charged particles. Additional gravitational losses occur for the larger-diameter particles due to their inertia and ability to deviate from streamlines; however, these losses would not explain why the peak charge state was lower only when the 12 μA ionizer current was used. It is therefore assumed that the drop in charge state for 2 and 3 μm particles charged using a 12 μA ionizer current can be attributed to electrostatic deposition, occurring due to the particles' highly charged state.

The same trend in peak particle charge was observed for the inverted results, with two approximately linear sections: minimally increasing charge states for the 0.49, 0.8, and 1 μm particles, and a significant increase in peak charge state for the 1.6, 2, and 3 μm particles. As for the non-inverted results, there was a drop in peak charge state for the 2 and 3 μm particles charged with an ionizer current of 12 μA.

Between the two results, there was a noticeable drop in the peak charge state. This was particularly true for the larger particle sizes, which were able to obtain much larger charge states overall. For instance, for nearly all the particles of diameter 1 μm or smaller, the magnitude of the charge state decrease was less than 10, while for the larger particle sizes, the decrease was usually at least 20. For all instances, the drop in charge state is caused by the DMA transfer function in the inversion process. The transfer function, as illustrated by Figure 15, will encompass an increasingly wide band of charge states as the particle size increases. Even for the smallest tested particle size, 0.49 μm, the transfer function has a set width, with values falling across several charge states. The process used to determine the state of charge for the non-inverted data essentially considers only the "peak" of the transfer function; this

single value fails to capture the intricacies of DMA operation. Once these elements are accounted for with the inversion, the charge state will tend to decrease, to reflect the true behavior of the DMA.

Discussion – Additional Considerations

From the results presented above, there are additional elements that can be discussed further, including the limits of the experimental setup on the data and the shape and width of the distributions.

Manipulation of Experimental Setup

One of the limitations of this work was the experimental setup used for this investigation. The setup was bounded by several system factors, including the maximum DMA voltage which could be safely used, the sheath flowrate of the DMA, and the dimensions of the DMA, as shown by Equation 1. For these experiments, a maximum DMA voltage of approximately 7 kV limited the minimum electrical mobility which could be obtained at each particle size. If the voltage limit were increased, the lower limit of electrical mobilities which can be transmitted by the DMA would correspondingly decrease. This lower-limit electrical mobility value will correspond with a charge state minimum, for a given particle size, which can be observed at the maximum DMA voltage.

Figure 28 shows the minimum particle charge states that can be theoretically transmitted and measured by systems with maximum operating voltages of 7, 8, and 10 kV, as a function of particle diameter.

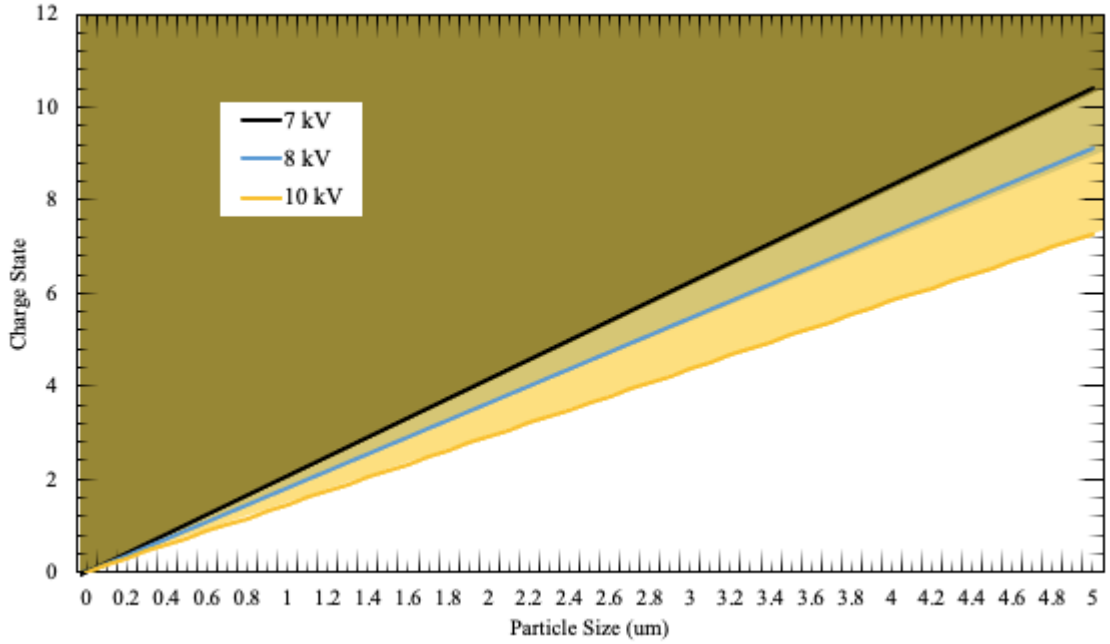

Figure 28. Lower bound of charge state, presented as a function of particle size. Data is shown for a DMA where the max operating voltage is 7, 8, and 10 kV. The attainable charge states are shaded, illustrating that above the lines for each voltage, all charge states for a given particle size could be transmitted and analyzed. Below the lines, transmission is not possible, per DMA theory (Equations 1-4).

The same limitations are true depending on the physical characteristics of the DMA itself, particularly its length. Assuming the other dimensions, specifically the inner and outer radii values, remain constant, then a similar plot of the measurable electrical mobilities can be constructed as a function of the DMA length. As for the applied DMA voltage, the relationship between electrical mobility and the physical DMA length (called "effective length," or L_{eff}) is governed by Equation 1. Figure 29 shows the range of electrical mobilities for which particle transmission through the DMA can occur, given a certain DMA length.

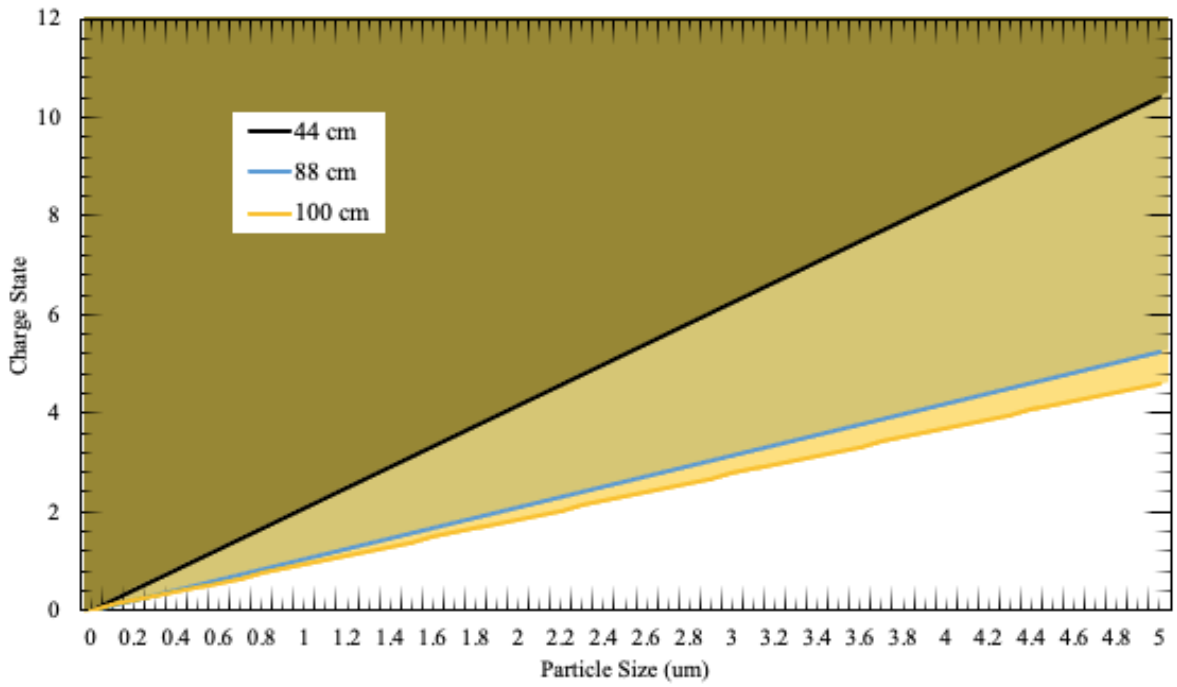

Figure 29. Lower bound of charge state, presented as a function of particle size. Data is shown for a DMA with a length of 44 cm (standard long-DMA length), 88 cm, and 100 cm. The attainable charge states are shaded, illustrating that above the lines for each voltage, all charge states for a given particle size could be transmitted and analyzed. Below the lines, transmission is not possible, per DMA theory (Equations 1-4).

These results show that with varied system parameters, it is theoretically possible to transmit even larger particles than were tested in this investigation. Additionally, as parameters are further tuned, said particles do not need to be as highly charged, which makes experimental transmission and analysis increasingly simple.

Shape and Width of Data

As discussed with respect to the charge fraction results, both the inverted and non-inverted

results tended to have a positively, or rightly, skewed shape, with a long tail to the right side of the distribution. This shape can be attributed to the method of particle charging and the electrostatic deposition that is theorized to occur for particles carrying an extremely high charge. An increased charge state could also be applied by increasing the ionizer current level, as was done in this investigation; however, electrostatic deposition is assumed to occur for highly charged particles, such as the 2 and 3 μm particles tested at an ionizer current of 12 μA. Electrostatic deposition may be difficult to mitigate and could be a limiting factor for analysis.

With additional investigation, the width of the distributions could also be tuned by adjusting the system operating parameters, such as the DMA sheath flow rate. While the width of the distributions will tend to broaden with increasing particle size (just as the DMA transfer function is wider for larger particles), there is some degree of optimization that could be achieved with experimental system adjustments.

Conclusion

The results obtained in this investigation demonstrate the potential for the novel combination of a Differential Mobility Analyzer (DMA) and an Optical Particle Spectrometer (OPS) to analyze the charge distributions of supermicrometer particles. Using a unipolar ionizer, particles were able to achieve sufficient charge states for successful transmission through the DMA, as shown here for particles up to 3 μm in diameter. Charge state distributions, determined as a function of particle size, allowed for a thorough understanding of particle charging using corona-generated ions, and the use of an inversion regime allowed the results to account for the transfer function of the DMA.

The measured distributions revealed that the distributions tended to have a positively skewed shape, with an increased probability of attaining relatively lower elementary charge states. The charge fraction was a key parameter of interest, and these results clearly illustrate the skewed behavior of the data. The definition of the charge fraction is the probability that a particle will have a given state of charge; the charge fraction results likely showed a positive-skew behavior due to the method of charging. Particles were charged via random collisions with ions experiencing Brownian motion. The experimental results confirm that with additional corona current in the ionizer, additional ion generation occurred, resulting in increased particle charge states. The relatively high measured charge states confirm that the method of charging is effective, but it could potentially be improved via system modifications that would allow for additional ion generation or more time for particle collisions. An additional cause for the skewed distribution shape is the likely occurrence of electrostatic deposition, resulting in increased particle losses for particles carrying higher charge states.

While this would be difficult to mitigate, it would improve the transmission of highly charged particles and could change the distribution shape to be more normally distributed.

For each of the tested experimental conditions, which included six particle sizes and three ionizer current levels, a peak charge state value was identified, corresponding to the charge state at which the highest particle concentration or charge fraction was obtained. A clear trend was demonstrated for both non-inverted and inverted results, with the peak charge state increasing as a function of particle size. Comparing results at the same particle size, the peak charge state also tended to increase as the ionizer current was increased. A notable exception to this trend was for 2 and 3 μm particles charged with an ionizer current of 12 μA, for which a drop in peak charge state was observed. This drop is assumed to be caused by increasing electrostatic deposition at higher charge states. Electrostatic deposition appears to be a factor that would become a more pressing concern with additional particle charging and could be a limitation on maximum particle charge.

Between the non-inverted and inverted results, particle charge states were observed to drop overall. The inversion process accounts for the DMA transfer function, which is the probability that a particle of a given mobility (size and charge) will successfully traverse the electrostatic classifier. The transfer function will enclose several unit charge states, regardless of particle size; the non-inverted method of charge state determination will capture only a single value of the charge state. As the particle size increases, the transfer function widens, introducing additional error into the non-inverted results for particles larger than 1 μm. By including the effects of the transfer function, the inverted results more fully represent the physical operation of the DMA; however, this also causes a decrease in the charge state.

Additional analysis of the experimental setup was conducted, to investigate how results might change with varied DMA conditions. A limiting factor of this investigation was the minimum charge state which could be obtained, as controlled by the maximum DMA voltage and the DMA length. It was found that increasing the maximum DMA voltage which could be applied would substantially decrease the minimum charge state that a particle would require to be transmitted through the DMA. The same phenomenon was observed with an increased DMA length; creating a longer DMA than the existing "long DMA", which has not previously been attempted, would allow for the transmission of particles with lower minimum charge states than is currently possible. These improvements could be important for use with even larger particles than were tested in this work, as the particles would not require extremely high charge levels for successful transmission.

Future work in this area could expand the applications of the system to increasingly large supermicrometer particles, up to the optical limits of the OPS. Additional investigation with an Aerodynamic Particle Spectrometer (APS) could allow for a further expansion of particle size limits, provided particle transmission continues to be possible. Further investigation into the method's use for larger particles, with the potential to decrease the need for excessive particle charging, would confirm its viability in additional industries and applications. The analysis of polydisperse aerosols is another future direction, which would require only an extension of the analysis methods to multiple particle sizes for each test. Finally, testing could be extended to powders, which would have applications in the printing industry.

Bibliography

1. S. Matsusaka, “Control of Particle Tribocharging,” *KONA Powder and Particle Journal*, vol. 29, pp. 27–38, 2011.
2. B. Düsenberg, S.-P. Kopp, F. Tischer, S. Schrüfer, S. Roth, J. Schmidt, M. Schmidt, D. W. Schubert, W. Peukert, and A. Bück, “Enhancing photoelectric powder deposition of polymers by Charge Control Substances,” *Polymers*, vol. 14, no. 7, p. 1332, 2022.
3. W. H. Hartung and C. T. Avedisian, “On the electrodynamic balance,” *Proceedings of the Royal Society of London. Series A: Mathematical and Physical Sciences*, vol. 437, no. 1900, pp. 237–266, 1992.
4. F. Zheng, X. Qu, and E. J. Davis, “An octopole electrodynamic balance for three-dimensional microparticle control,” *Review of Scientific Instruments*, vol. 72, no. 8, pp. 3380–3385, Jul. 2001.
5. M. K. Mazumder, R. E. Ware, T. Yokoyama, B. J. Rubin, and D. Kamp, “Measurement of particle size and electrostatic charge distributions on toners using E-SPART Analyzer,” *IEEE Transactions on Industry Applications*, vol. 27, no. 4, pp. 611–619, 1991.
6. S. Matsusaka, M. Oki, and H. Masuda, “Control of electrostatic charge on particles by impact charging,” *Advanced Powder Technology*, vol. 18, no. 2, pp. 229–244, 2007.
7. D. Witten, “Millikan's oil drop experiment,” *Mathwizurd*, 15-Feb-2017. [Online]. Available: https://www.mathwizurd.com/physics/2017/2/14/millikans-oil-drop-experiment. [Accessed: 30-Mar-2023].
8. J. Clark, “The Mass Spectrometer,” *The mass spectrometer - how it works*, 2019. [Online]. Available: https://www.chemguide.co.uk/analysis/masspec/howitworks.html. [Accessed: 30-Mar-2023].
9. T. S. Chadha, S. Chattopadhyay, C. Venkataraman, and P. Biswas, “Study of the charge distribution on liposome particles aerosolized by air-jet atomization,” *Journal of Aerosol Medicine and Pulmonary Drug Delivery*, vol. 25, no. 6, pp. 355–364, 2012.
10. R. H. Epping and A. Kuettner, “Free Air Beam in an electric field for determination of the electrostatic charge of powders between 1 and 200µm,” *Journal of Electrostatics*, vol. 55, no. 3-4, pp. 279–288, 2002.
11. M. D. Petters, “DMA,” *Markus D. Petters | DMA*. [Online]. Available: https://mdpetters.github.io/software/2_software/. [Accessed: 02-Apr-2023].
12. B. Y. H. Liu, D. Y. H. Pui, K. T. Whitby, D. B. Kittelson, Y. Kousaka, and R. L. McKenzie, "The aerosol mobility chromatograph: A new detector for sulfuric acid aerosols," *Atmospheric Environment*, vol. 12, no. 1-3, pp. 99-104, 1978.
13. P. H. McMurry, H. Takano, and G. R. Anderson, “Study of the Ammonia (Gas) – Sulfuric Acid (Aerosol) Reaction Rate,” *Environmental Science Technology*, vol. 17, pp. 347-352, 1983.
14. E. O. Knutson, “Extended electrical mobility method for measuring aerosol particle size and concentration,” *Fine Particles*, pp. 739-762, 1976.

15. W. A. Hoppel, “Determination of the aerosol size distribution from the mobility distribution of the charged fraction of aerosol,” *Journal of Aerosol Science*, vol. 9, no. 1, pp. 41-54, 1978.
16. H. Fissan, C. Helsper, A. Kapadia, and B. Y. H. Liu, “Data inversion by simplex minimization for the electrical aerosol analyzer,” *Aerosol Science and Technology*, vol. 1, no. 2, pp. 135-146, 1982.
17. A. Plomp, H. M. ten Brink, H. Spoelstra, and J. F. van de Vate, “A high-resolution electrical mobility aerosol spectrometer (MAS), *Journal of Aerosol Science*, vol. 14, no. 5, pp. 589-597, 1983.
18. H. G. Scheibel, A. Hussin, K. H. Becker, and J. Porstendörfer, “Bipolar diffusion charging of aerosol particles – I: experimental results within the diameter range 4-30 nm,” *Journal of Aerosol Science*, vol. 14, no. 5, pp. 671-677, 1983.
19. Y. Kousaka, K. Okuyama, and M. Adachi, “Determination of particle size distribution of ultra-fine aerosols using a differential mobility analyzer,” *Aerosol Science and Technology*, vol. 4, no. 2, pp. 209-225, 1985.
20. M. Sahu, J. Park, and P. Biswas, “In situ charge characterization of TiO_2 and Cu-TiO_2 nanoparticles in a flame aerosol reactor,” *Journal of Nanoparticle Research*, vol. 14, p. 678, 2012.
21. G. Biskos, K. Reavell, and N. Collings, “Unipolar diffusion charging of aerosol particles in the transition regime,” *Journal of Aerosol Science*, vol. 26, no. 2, 2005.
22. H. Kaminski, T. A. J. Kuhlbusch, H. Fissan, L. Ravi, H-G. Horn, H-S. Han, R. Caldow, and C. Asbach, “Mathematical description of experimentally determined charge distributions of a unipolar diffusion charger,” *Aerosol Science and Technology*, vol. 46, no. 6, pp. 708-716, 2012.
23. A. Järvinen, P. Heikkilä, and J. Yli-Ojanperä, “Particle charge-size distribution measurement using a differential mobility analyzer and an electrical low pressure impactor,” *Aerosol Science and Technology*, vol. 51, no. 1, pp. 20-29, 2017.
24. M. Domat, F. E. Kruis, and J. M. Fernandez-Diaz, “Determination of the relevant charging parameters for the modeling of unipolar chargers,” *Journal of Aerosol Science*, vol. 71, pp. 16-28, 2014.
25. B. Y. H. Liu and D. Y. H. Pui, “Equilibrium bipolar charge distribution of aerosols,” *Journal of Colloid and Interface Science*, vol. 49, no. 2, pp. 305-312, 1974.
26. M. M. Maricq, “Bipolar diffusion charging of soot aggregates,” *Aerosol Science and Technology*, vol. 42, no. 4, 2008.
27. T. J. Johnson, R. T. Nishida, M. Irwin, J. P. R. Symonds, J. S. Olfert, and A. M. Boies, “Measuring the bipolar charge distribution of nanoparticles: review of methodologies and development using the aerodynamic aerosol classifier,” *Journal of Aerosol Science*, vol. 143, 2020.
28. A. Biermann and W. Bergman, “Measurement of aerosol concentration as a function of size and charge,” *Aerosol Science and Technology*, vol. 3, no. 3, pp. 293-304, 1984.
29. E. P. Emets, V. A. Kascheev, and P. P. Poluektov, “Simultaneous measurement of aerosol particle charge and size distributions,” *Journal of Aerosol Science*, vol. 22, no. 3, pp. 389-394, 1991.

30. B. Forsyth, B. Y. H. Liu, and F. J. Romay, “Particle charge distribution measurement for commonly generated laboratory aerosols,” *Aerosol Science and Technology*, vol. 28, no. 6, pp. 489-501, 1998.
31. M. Adachi, Y. Kousaka, and K. Okuyama, “Unipolar and bipolar diffusion charging of ultrafine aerosol particles,” *Journal of Aerosol Science*, vol. 16, no. 2, pp. 109-123, 1985.
32. K. T. Whitby, “Generator for producing high concentrations of small ions,” *Review of Scientific Instruments*, vol. 32, no. 12, 1961.
33. P. Intra and N. Tippayawong, “An overview of unipolar charger developments for nanoparticle charging,” *Aerosol and Air Quality Research*, vol. 11, pp. 187-209, 2011.
34. E. O. Knutson and K. T. Whitby, “Aerosol classification by electric mobility: apparatus, theory, and applications,” *Journal of Aerosol Science*, vol. 6, no. 6, pp. 443-451, 1975.
35. TSI Particle Instruments, “Series 3080 Electrostatic Classifiers,” “*Operation and Service Manual*,” P 1933792 (2012).
36. M. D. Allen and O. G. Raabe, “Slip correction measurements of spherical solid aerosol particles in an improved Millikan apparatus,” *Aerosol Science and Technology*, vol. 4, no. 3, 1985.
37. J. Morán, L. Li, H. Ouyang, Y. Qiao, B. A. Olson, and C. J. Hogan, “Characterization of the bidimensional size and charge distribution of sub- and supermicrometer particles in an electrostatic precipitator,” *Powder Technology*, 2023, Under Review.
38. C. R. Vogel, “Computational methods for inverse problems,” *Society for Industrial and Applied Mathematics*, 2002.
39. P. C. Hansen, “The L-curve and its use in the numerical treatment of inverse problems,” *SINTEF*, 1999.
40. A. Reineking and J. Porstendörfer, “Measurements of particle loss functions in a differential mobility analyzer (TSI, Model 3071), for different flow rates, *Aerosol Science and Technology*, vol. 5, no. 4, 1986.
41. M. R. Stolzenburg and P. H. McMurry, “Equations governing single and tandem DMA configurations and a new lognormal approximation to the transfer function,” *Aerosol Science and Technology*, vol. 42, no. 6, 2008.
42. C. Hagwood, “The DMA transfer function with Brownian motion a trajectory/Monte-Carlo approach,” *Aerosol Science and Technology*, vol. 30, no. 1, 1999.
43. Stolzenburg, M. R., 1988, “An ultrafine aerosol size distribution measuring system,” Ph.D. dissertation, University of Minnesota, Minneapolis, MN.
44. W. Yang, J. Kangasluoma, M. Attoui, F. Jiaxi, H. Junninen, M. Kulmala, T. Petäjä, and P. Biswas, “The high charge fraction of flame-generated particles in the size range below 3 nm measured by enhanced particles detectors,” *Combustion and Flame*, vol. 176, pp. 72-80, 2017.
45. M. M. Maricq, “Size and charge of soot particles in rich premixed ethylene flames,” *Combustion and Flame*, vol. 137, no. 3, pp. 340-350, 2004.
46. R. Gopalakrishnan and H. S. Chahl, “High potential, near free molecular regime Coulombic collisions in aerosols and dusty plasmas,” *Aerosol Science and Technology*, vol. 53, no. 8, pp. 933-957, 2019.

Appendices

Appendix A – Dimensioned Unipolar Ionizer Schematics

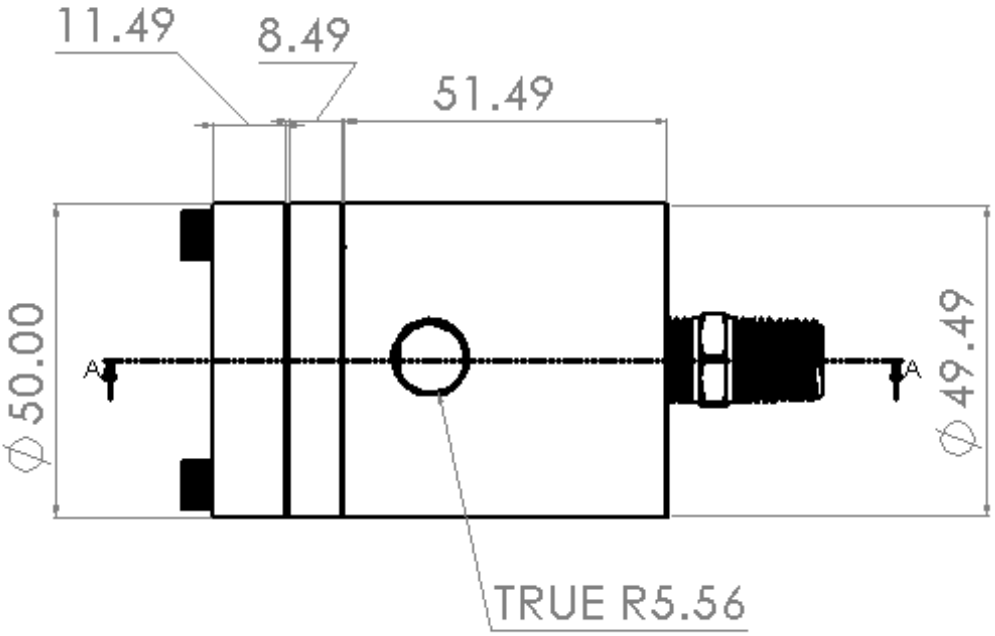

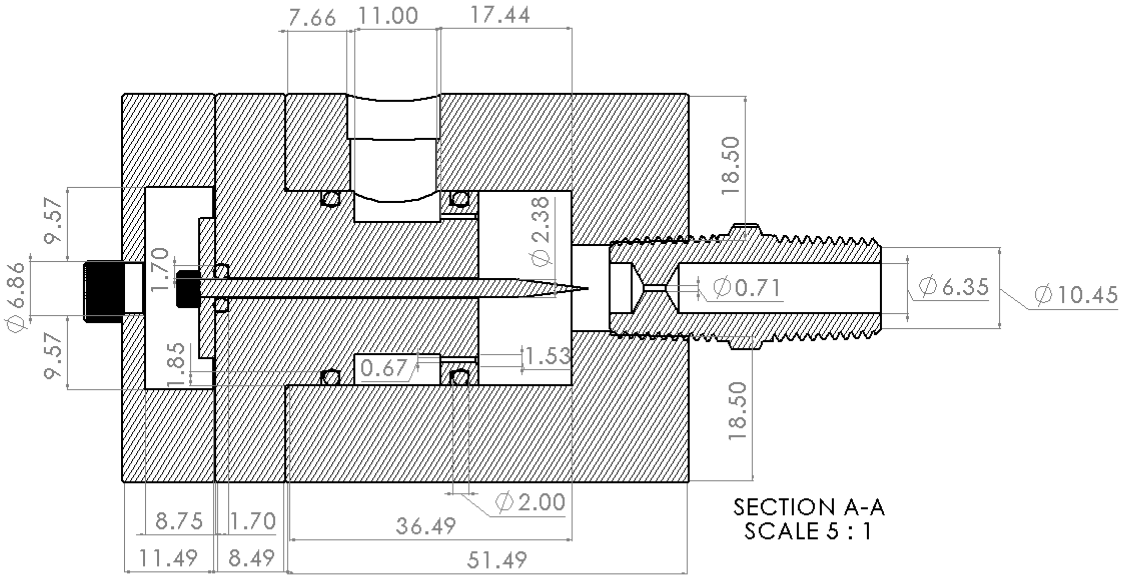

Appendix B – Image Permissions

Reproduced images are used with permission, either implicitly (when originally published on a website) or with express publisher permission. All reproduced images are attributed to their original source via citation. Publisher permissions can be found below.

MARY ANN LIEBERT, INC. LICENSE
TERMS AND CONDITIONS

Mar 23, 2023

This Agreement between University of Minnesota -- Sarah Ley ("You") and Mary Ann Liebert, Inc. ("Mary Ann Liebert, Inc.") consists of your license details and the terms and conditions provided by Mary Ann Liebert, Inc. and Copyright Clearance Center.

License Number	5514580084364
License date	Mar 23, 2023
Licensed Content Publisher	Mary Ann Liebert, Inc.
Licensed Content Publication	Journal of Aerosol Medicine and Pulmonary Drug Delivery
Licensed Content Title	Study of the Charge Distribution on Liposome Particles Aerosolized by Air-Jet Atomization
Licensed Content Author	Tandeep S. Chadha, Saptarshi Chattopadhyay, Chandra Venkataraman, et al
Licensed Content Date	Dec 1, 2012
Licensed Content Volume	25
Licensed Content Issue	6
Type of Use	Dissertation/Thesis
Requestor type	author of the original work
Format	electronic
Portion	figures/tables
Number of figures/tables	1
Distribution quantity	50
Title	Charge Distribution Inversion for Supermicron Particles via Differential Mobility Analysis and Optical Particle Spectrometry
Institution name	University of Minnesota
Expected presentation date	May 2023
Portions	Figure 1, Schematic diagram of the TDMA setup for measuring charge distribution of particles.
Requestor Location	University of Minnesota 117 27th Ave SE Unit 566 MINNEAPOLIS, MN 55414 United States Attn: University of Minnesota
Total	0.00 USD

Terms and Conditions

Mary Ann Liebert, Inc. publishers Terms and Conditions

1. Introduction

The publisher for this copyrighted material is Mary Ann Liebert, Inc. publishers. By clicking "accept" in connection with completing this licensing transaction, you agree that the following terms and conditions apply to this transaction (along with the Billing and Payment terms and conditions established by Copyright Clearance Center, Inc. ("CCC"), at the time that you opened your Rightslink account and that are available at any time at https://myaccount.copyright.com).

2. Limited License

Publisher hereby grants to you a non-exclusive license to use this material. Licenses are for one-time use only with a maximum distribution equal to the number that you identified in the licensing process and any electronic posting is limited to the period committed to at the time of purchase.

3. Geographic Rights: Scope

Licenses may be exercised anywhere in the world.

4. Jurisdiction:

This agreement shall be governed by and construed in accordance with the laws of the state of New York, without giving effect to any principles of conflicts of law. If any provision of this agreement shall be unlawful, void, or for any reason unenforceable, then that provision shall be deemed severable from this agreement and shall not affect the validity and enforceability of any remaining provisions. This is the entire agreement between the parties relating to the subject matter herein and shall not be modified except in writing, signed by both parties.

5. Altering/Modifying Material: Not Permitted

You may not alter or modify the material in any manner without the explicit approval of the Publisher.

6. Reservation of Rights

Publisher reserves all rights not specifically granted in the combination of (i) the license details provided by you and accepted in the course of this licensing transaction, (ii) these terms and conditions and (iii) CCC's Billing and Payment terms and conditions.

7. License Contingent on Payment

While you may exercise the rights licensed immediately upon issuance of the license at the end of the licensing process for the transaction, provided that you have disclosed complete and accurate details of your proposed use, no license is finally effective unless and until full payment is received from you (either by publisher or by CCC) as provided in CCC's Billing and Payment terms and conditions. If full payment is not received on a timely basis, then any license preliminarily granted shall be deemed automatically revoked and shall be void as if never granted. Further, in the event that you breach any of these terms and conditions or any of CCC's Billing and Payment terms and conditions, the license is automatically revoked and shall be void as if never granted. Use of materials as described in a revoked license, as well as any use of the materials beyond the scope of an unrevoked license, may constitute copyright infringement and publisher reserves the right to take any and all action to protect its copyright in the materials.

8. Copyright Notice: Disclaimer

You must include the following copyright and permission notice in connection with any reproduction of the licensed material:" The publisher for this copyrighted material is Mary Ann Liebert, Inc. publishers."

9. Warranties: None

Publisher makes no representations or warranties with respect to the licensed material and adopts on its own behalf the limitations and disclaimers established by CCC on its behalf in its Billing and Payment terms and conditions for this licensing transaction.

10. Indemnity

You hereby indemnify and agree to hold harmless publisher and CCC, and their respective officers, directors, employees and agents, from and against any and all claims arising out of your use of the licensed material other than as specifically authorized pursuant to this license.

11. No Transfer of License

This license is personal to you and may not be sublicensed, assigned, or transferred by you to any other person without publisher's written permission.

12. No Amendment Except in Writing

This license may not be amended except in writing signed by both parties (or, in the case of publisher, by CCC on publisher's behalf).

13. Objection to Contrary Terms

Publisher hereby objects to any terms contained in any purchase order, acknowledgment, check endorsement or other writing prepared by you, which terms are inconsistent with these terms and conditions or CCC's Billing and Payment terms and conditions. These terms and conditions, together with CCC's Billing and Payment terms and conditions (which are incorporated herein), comprise the entire agreement between you and publisher (and CCC) concerning this licensing transaction. In the event of any conflict between your obligations established by these terms and conditions and those established by CCC's Billing and Payment terms and conditions, these terms and conditions shall control.

v1.1

Questions? customercare@copyright.com.